RSC Sustainability

PAPER

View Article Online
View Journal | View Issue

Cite this: *RSC Sustainability*, 2026, 4, 1912

Green synthesis of EuCN S-scheme photocatalysts *via Centella asiatica* extract for enhanced MB photodegradation and H_2O_2 photoproduction: DFT investigation and mechanistic insights

Tran Dang Khoa,[abd] Nguyen Phi Hao,[abd] Le Thanh Hoang Duc,[abd] Pham Duc Nghi,[abd] Nguyen Hung Vu,[abd] Dang Thanh Cong Minh,[abd] Tran Nguyen Cam Nhung,[abd] Nguyen Minh Phi,[cd] Tran Thi Thu Hanh,[cd] Nguyen Minh Hung[abd] and Nguyen Huu Hieu *[abd]

Received 18th January 2026
Accepted 23rd February 2026

DOI: 10.1039/d6su00035e

rsc.li/rscsus

Driven by the growing demand for sustainable solutions in environmental remediation and solar energy conversion, a green synthetic strategy was employed to prepare europium oxide (Eu_2O_3) using *Centella asiatica* extract, followed by integration with graphitic carbon nitride (CN) to fabricate EuCN composite photocatalysts. Characterization techniques including FTIR, XRD, FE-SEM, EDX, UV-DRS, BET, TEM, SAED, and XPS confirmed the structure and properties. Optical and electrochemical features were further evaluated using PL, Mott–Schottky, *I*–*t*, and EIS analyses. The composition of the extract was confirmed by HPLC. The as-prepared EuCN composites demonstrated remarkable photocatalytic performance, achieving 93.82% degradation of methylene blue and 233.73 μM hydrogen peroxide generation under visible light irradiation. The effects of key operational parameters, including catalyst dosage, pH, and pollutant concentration, were examined to optimize the photocatalytic response. Mechanistic analysis combined with density functional theory (DFT) calculations indicated that the enhanced photocatalytic activity is governed by an S-scheme charge-transfer pathway, supported by work function alignment and interfacial electronic structure regulation. The redox cycling between Eu^{3+} and Eu^{2+} associated with 4f orbital characteristics further contributes to charge separation and preservation of strong redox potentials. These results demonstrate the potential of EuCN composites for multifunctional applications in environmental purification and solar-to-chemical energy conversion.

Sustainability spotlight

This work presents a green and sustainable strategy for developing high-performance photocatalysts by integrating plant-mediated synthesis with advanced semiconductor engineering. Europium oxide was synthesized using *Centella asiatica* leaf extract as a renewable bio-reducing agent and subsequently coupled with graphitic carbon nitride to form EuCN composites. The approach avoids toxic reagents, valorizes local biomass resources, and aligns with circular economy principles. The resulting photocatalyst demonstrates dual environmental functionality, achieving efficient visible-light-driven degradation of methylene blue and photocatalytic generation of hydrogen peroxide, an environmentally benign oxidant. Mechanistic investigations supported by density functional theory reveal that Eu^{3+}/Eu^{2+} redox cycling enables an effective S-scheme charge-transfer pathway, enhancing charge separation while preserving strong redox potentials. By combining low-impact synthesis, material durability, and multifunctional photocatalytic performance, this study contributes to sustainable solutions for wastewater remediation and solar-to-chemical energy conversion.

1. Introduction

The rapid pace of industrialization and urban expansion has led to severe environmental pollution and an intensifying global energy crisis.[1] Among various pollutants, the contamination of water by synthetic dyes represents a particularly critical issue. Methylene blue (MB) is a widely used thiazine dye in the textile, leather, paper, and medical industries and is a major concern due to its high toxicity, chemical stability, non-biodegradability, and potential carcinogenicity.[2,3] Conventional wastewater

---

[a] *VNU-HCM, Key Laboratory of Chemical Engineering and Petroleum Processing (Key CEPP Lab), Ho Chi Minh City University of Technology (HCMUT), 268 Ly Thuong Kiet Street, Dien Hong Ward, Ho Chi Minh City, Vietnam. E-mail: nhhieubk@hcmut.edu.vn*

[b] *Faculty of Chemical Engineering, Ho Chi Minh City University of Technology (HCMUT), 268 Ly Thuong Kiet Street, Dien Hong Ward, Ho Chi Minh City, Vietnam*

[c] *Department of Applied Physics, Ho Chi Minh University of Technology, 268 Ly Thuong Kiet Street, Dien Hong Ward, Ho Chi Minh City, Vietnam*

[d] *Vietnam National University Ho Chi Minh City (VNU), Linh Xuan Ward, Ho Chi Minh City, Vietnam*

treatment methods, including adsorption, coagulation, and biological degradation, often exhibit limited effectiveness in completely removing MB and are frequently associated with high operational costs and the generation of secondary pollutants.[4] Photocatalysis has emerged as a promising green technology that leverages solar energy to produce reactive oxygen species capable of breaking down persistent organic pollutants like MB into harmless byproducts.[4,5] This strategy not only enhances degradation efficiency but also supports sustainability objectives by coupling pollutant remediation with clean energy generation processes, including the photoproduction of hydrogen (H_2), hydrogen peroxide (H_2O_2), ammonia (NH_3), *etc.*[6,7] Among these products, H_2O_2 is regarded as an environmentally benign oxidant widely applied in wastewater treatment, disinfection, and as a promising energy carrier for emerging fuel-cell technologies.[8]

Among photocatalytic materials, graphitic carbon nitride (CN) has garnered considerable interest due to its suitable bandgap, excellent thermal and chemical stability, and ease of synthesis from nitrogen-rich precursors.[9] However, its photocatalytic performance is limited by intrinsic drawbacks such as fast recombination of charge carriers, low specific surface area, and poor conductivity.[10] To address these limitations, heterojunction engineering by coupling CN with complementary semiconductors has emerged as a viable strategy.[11] Recent advances further highlight that rational interface design, including S-scheme configuration, Schottky junction formation, and interfacial chemical bonding, can establish internal electric fields that facilitate directional electron transfer and suppress charge recombination, thereby enhancing visible-light redox performance.[12,13] In parallel, interfacial electronic regulation combined with photothermal synergy has been reported to accelerate solar H_2 evolution, where band structure modulation and internal electric field formation cooperate to enhance carrier migration efficiency.[14] In this context, recent developments in heterogeneous photocatalysis have increasingly emphasized the integration of interfacial electronic regulation with practical structural engineering to simultaneously advance environmental remediation and green energy production. For example, the construction of a self-floating S-scheme heterojunction anchored on conductive carbon fiber substrates has been demonstrated to enhance charge separation efficiency while enabling convenient catalyst recovery and stable pollutant degradation in complex aqueous systems.[15] Furthermore, the incorporation of interfacial electron donors within S-scheme architectures has been reported to reinforce internal electric field formation and promote selective charge recombination, thereby preserving strong redox potentials and significantly improving visible-light-driven hydrogen evolution performance.[16] These representative studies reflect the current research trend toward rational heterostructure design that couples efficient charge dynamics with practical applicability. Among the various modification strategies, the integration of CN with metal oxides such as CuO, ZnO, SnO_2, CeO_2, and Eu_2O_3 represents one of the most effective approaches to enhance interfacial charge separation, extend visible-light absorption, and reinforce surface redox activity.[17] Ho *et al.* reported the green synthesis of g-C_3N_4/CeO_2 nanocomposites using *Cleistocalyx operculatus* leaf extract, achieving 95.70% methylene blue degradation under simulated sunlight. The enhanced performance was attributed to the narrowed band gap (2.49 eV), high surface area, and improved charge separation resulting from the synergistic interaction between g-C_3N_4 and CeO_2.[18] Chen *et al.* constructed Dy_2O_3/g-C_3N_4 heterojunctions *via* a pore impregnation method, demonstrating significantly enhanced photocatalytic hydrogen evolution activity. The optimized 3% DyO/CN sample achieved a hydrogen evolution rate of 9.9 mmol g^{-1} h^{-1}, nearly three times higher than that of pristine g-C_3N_4. The improved performance was attributed to efficient charge separation at the heterointerface and the introduction of nitrogen vacancies, which broadened light absorption and facilitated carrier migration.[19] Jing *et al.* enhanced the visible-light photocatalytic hydrogen production of Dy_2O_3/g-C_3N_4 by incorporating biomass-derived graphene-like carbon from *Enteromorpha prolifera*. The introduction of graphene-like carbon improved the surface area, facilitated electron transport, and promoted charge separation within the heterojunction. The resulting ternary composite achieved a hydrogen evolution rate up to 723.57 μmol g^{-1} h^{-1}, which was more than three times higher than that of pristine Dy_2O_3, demonstrating the effectiveness of biomass-assisted interfacial engineering for improving photocatalytic performance.[20]

Europium oxide (Eu_2O_3) is particularly attractive due to its wide bandgap ($E_g = 4.3$ to 4.5 eV), which enables favorable band alignment with CN. The 4f electronic configuration of Eu^{3+} ions contributes to unique luminescent properties, including photon upconversion that enhances visible light harvesting.[21] These properties collectively enhance the photocatalytic activity and stability of Eu_2O_3/CN heterostructures. Traditional synthesis of metal oxides like Eu_2O_3 typically involves harsh chemicals, high temperatures, and complex procedures, thereby raising concerns about environmental safety and process sustainability.[22] In recent years, plant-mediated synthesis has emerged as an eco-friendly alternative, utilizing phytochemicals from natural extracts as reducing and stabilizing agents under mild reaction conditions. This green chemistry approach not only reduces toxic byproducts but also aligns with the principles of the circular economy by utilizing agricultural waste.[23]

Centella asiatica (*C. asiatica*) is a medicinal plant native to Vietnam and commonly consumed as a leafy vegetable, representing a valuable biomass source for green synthesis owing to its abundance and high content of bioactive compounds.[24] While its leaves are widely used in traditional medicine and local cuisine, the remaining biomass is frequently discarded. Notably, *C. asiatica* is rich in flavonoids, polyphenols, and triterpenoid compounds that exhibit strong reducing and metal-chelating properties. Compared with other commonly used plant extracts in phytosynthesis, *C. asiatica* contains a relatively higher proportion of phenolic constituents and multifunctional hydroxyl groups, which favor efficient metal ion coordination and controlled nucleation during nanoparticle formation.[25] In addition, the presence of triterpenoids provides additional surface-active functionalities that may contribute to particle stabilization. Despite these promising chemical characteristics, the potential of these bioactive molecules in the green synthesis of nanomaterials remains largely underexplored.[26] Harnessing these natural reducers for the biosynthesis of Eu_2O_3 not only contributes to sustainable biomass valorization but also introduces functional groups that can enhance the electrochemical and photocatalytic performance of the resulting composites.

In the present work, a bio-assisted strategy was employed to synthesize europium oxide (Eu_2O_3) using *C. asiatica* leaf extract, and the resulting material was combined with CN to construct a Eu_2O_3/CN heterostructure (EuCN). The composites were thoroughly characterized using Fourier-transform infrared spectroscopy (FTIR), X-ray diffraction (XRD), scanning electron microscopy (SEM), field-emission scanning electron microscopy (FE-SEM), transmission electron microscopy (TEM), selected area electron diffraction (SAED), Brunauer–Emmett–Teller (BET) surface area analysis, ultraviolet-visible diffuse reflectance spectroscopy (UV-DRS), photoluminescence (PL) spectroscopy, and X-ray photoelectron spectroscopy (XPS). The components of the extract were identified using high-performance liquid chromatography (HPLC). Electrochemical properties were assessed through Mott–Schottky analysis, transient photocurrent response (*I*–*t*), and electrochemical impedance spectroscopy (EIS). Photocatalytic performance was investigated through MB degradation and H_2O_2 production. Furthermore, radical scavenging experiments and density functional theory (DFT) calculations were conducted to gain deeper insight into the underlying photocatalytic mechanism.

2. Experimental

2.1. Materials and chemicals

Methylene blue ($C_{16}H_{18}ClN_3S$, 99%), melamine ($C_3H_6N_6$, 99%), urea (CH_4N_2O, 99%), sulfuric acid (H_2SO_4, 98%), methanol (CH_3OH, 99.5%), ethylene glycol ($C_2H_6O_2$, 99.9%), and potassium hydroxide (KOH, 85%) were obtained from Xilong. Disodium ethylenediaminetetraacetate dihydrate ($C_{10}H_{14}N_2Na_2O_8 \cdot 2H_2O$, 99%), *p*-benzoquinone ($C_6H_4O_2$, 98% (BQ)), potassium iodide (KI, 99.5%), mannitol ($C_6H_{14}O_6$, 99%), silver nitrate ($AgNO_3$, 99%), and potassium hydrogen phthalate ($C_8H_5KO_4$, 99.5% (KHP)) were obtained from Merck. Europium(III) nitrate hexahydrate ($Eu(NO_3)_3 \cdot 6H_2O$, 99%) was supplied by Shanghai Titan Scientific Co., Ltd, China. Ethanol (C_2H_5OH, 99.5%) was brought from the CEMACO company, Vietnam. Double distilled water (DW) was used throughout all the experiments. *C. asiatica* was collected from Sa Dec Ward, Dong Thap Province, Vietnam, as shown in Fig. S1.

2.2. Preparation of *Centella asiatica* extract

The extraction process of *C. asiatica* is illustrated in Fig. S2. Initially, the plant material was thoroughly rinsed with clean water to remove surface impurities, followed by two additional washes with distilled water. The cleaned samples were then completely dried in a drying cabinet to eliminate residual moisture. After drying, the *C. asiatica* was ground into a fine powder for storage and later use in the experiments. A measured 10 g portion of the powder was transferred into a 250 mL beaker, followed by the addition of 100 mL of DW. The mixture was heated at 50 °C for 1 h and subsequently subjected to sonication for an additional 1 h. The resulting aqueous extract was collected *via* vacuum filtration to remove solid residues and then stored at 4 °C for subsequent experimental procedures.

2.3. Synthesis of graphitic carbon nitride

Graphitic carbon nitride (CN) was synthesized *via* a simple thermal polymerization method adapted from our previous work.[27] In a typical procedure (Fig. S3), melamine and urea were mixed in a 1 : 1 weight ratio and thoroughly ground into a homogeneous powder. The mixture was then transferred into a covered crucible and subjected to thermal treatment at 550 °C for 4 h in ambient air. After naturally cooling to room temperature, the resulting yellow product was collected, repeatedly washed with deionized water to remove residual impurities, and subsequently dried at 50 °C.

2.4. Green synthesis of europium oxide

The synthesis of Eu_2O_3 is illustrated in Fig. S4. Briefly, 500 mg of $Eu(NO_3)_3 \cdot 6H_2O$ was dissolved in 50 mL of distilled water, followed by the addition of 100 mL of *C. asiatica* extract. The resulting mixture was stirred at 80 °C for 1 h to ensure uniform mixing. The suspension was transferred into a Teflon-lined stainless-steel autoclave and subjected to hydrothermal treatment at 200 °C for 6 h. After cooling to room temperature, the product was centrifuged, thoroughly washed with distilled water to remove residual ions, and dried in an oven. Finally, the obtained powder was calcined at 800 °C for 1 h to yield crystalline Eu_2O_3.

2.5. Synthesis of europium oxide-decorated on graphitic carbon nitride composites

Europium oxide-decorated on graphitic carbon nitride (EuCN) composites were synthesized *via* a simple sonication-assisted method, as shown in Fig. S5. In a typical synthesis, 1 g of CN was dispersed in 50 mL of distilled water and ultrasonicated for 1 h to achieve a uniform suspension. Subsequently, a predetermined amount of Eu_2O_3 was added, followed by an additional 1 h of sonication to ensure proper dispersion and interaction between the components. The resulting mixture was centrifuged, and the collected solid was dried at 60 °C. EuCN composites were prepared with Eu_2O_3 loadings of 5, 10, and 15% by weight relative to CN, and were denoted as 5EuCN, 10EuCN, and 15EuCN, respectively.

2.6. Characterization of materials

The functional groups present in the synthesized materials were identified using FTIR (Alpha-E, Bruker Optik GmbH, Ettlingen, Germany). The crystalline phases were analyzed by XRD (D2 Phaser, Bruker, Germany) employing Cu Kα radiation (λ = 0.1541 nm) over a 2θ range of 5–80°. Surface morphology and elemental composition were examined using FE-SEM (Hitachi

S4800, USA), EDX (Jeol-JMS 6490, Japan), TEM (JEM 2100, Jeol, Japan), and SAED (JEM 2100, Jeol, Japan). The chemical states and surface composition were further investigated by XPS (Nexsa G2, USA). Optical absorption characteristics were investigated using UV-DRS (V-770, JASCO, Japan). Specific surface area and pore size distribution were determined using BET analysis (Nova e4000, Quantachrome, USA). Photocatalytic performance was evaluated using UV-visible spectroscopy (UV-vis, Thermo Scientific, Thermal 220). Photoluminescence (PL) measurements were conducted using a spectrofluorometer (HORIBA Scientific, FluoroLog-5MAX) to investigate the recombination dynamics of photogenerated charge carriers. The composition of the extract was analyzed by HPLC (Shimadzu LC-40D XR Liquid Chromatography, Japan) and the procedure for HPLC is described in Section S6.

2.7. Evaluation of photocatalytic performance

2.7.1. Photodegradation of methylene blue. The photocatalytic activity of the synthesized materials was systematically assessed through the degradation of MB under irradiation from a 50 W halogen lamp as a simulated sunlight source. In each test, 30 mg of the photocatalyst was dispersed in an aqueous MB solution with an initial concentration of 10 ppm. Prior to illumination, the suspension was magnetically stirred in the dark for 30 minutes to ensure adsorption–desorption equilibrium. During irradiation, 3 mL samples were withdrawn at regular intervals of 30 minutes, followed by immediate filtration to eliminate any solid residues. The absorbance of MB at 664 nm was monitored using a UV-vis spectrophotometer. The degradation efficiency was calculated using eqn (1).

$$\text{Photodegradation effiency}(\%) = \frac{(C_0 - C_t)}{C_0} \times 100 \qquad (1)$$

where C_0 and C_t (ppm) are the initial concentration and concentration at time t of MB, respectively.

The effect of solution pH on the photodegradation of MB was examined by adjusting the pH using 0.01 M KOH and H_2SO_4, with precise measurements recorded *via* a Hanna HI98100 pH meter. In parallel, the impact of varying catalyst dosages and pollutant concentration on the photodegradation efficiency was systematically investigated to determine the optimal loading conditions. To elucidate the underlying degradation mechanism, the involvement of key reactive species, including (h^+), electrons (e^-), hydroxyl radicals ($^{\bullet}OH$), and superoxide radicals ($^{\bullet}O_2^-$), was analyzed using scavengers such as EDTA, $AgNO_3$, mannitol, and BQ, respectively. The reusability of the photocatalyst was assessed over successive photocatalytic cycles. After each cycle, 50 mg of the used material was separated by centrifugation, thoroughly washed with deionized water and ethanol to remove any adsorbed species or residues, and subsequently dried under ambient conditions prior to reuse in the next run.

2.7.2. Photoproduction of hydrogen peroxide. The photoproduction of H_2O_2 was systematically evaluated by dispersing 10 mg of the photocatalyst in 50 mL of 10% (v/v) sacrificial agent solution. Before illumination, the suspension was magnetically stirred in the dark for 30 minutes to establish adsorption–desorption equilibrium. Photoreactions were conducted under a 50 W LED light source, and aliquots (1 mL) of the reaction suspension were withdrawn at 30 min intervals. Each sample was subsequently filtered to remove any residual solids and mixed with 2 mL of an analytical reagent consisting of 0.4 M KI and 0.1 M KHP in a 1 : 1 volume ratio. After 30 minutes of the reaction under ambient conditions, the absorbance of the resulting mixture was recorded at 350 nm using a UV-vis spectrophotometer to determine the concentration of H_2O_2. The H_2O_2 concentration is determined using eqn (S1).

To optimize the photoproduction performance, the influence of various sacrificial electron donors, including ethylene glycol, ethanol, and methanol, was investigated. The reaction mechanism was investigated using appropriate scavengers: EDTA, $AgNO_3$, mannitol, and BQ. The effect of pH on the photocatalytic efficiency was systematically studied by adjusting the reaction medium with 0.01 M KOH or H_2SO_4, with the pH monitored using a Hanna HI98100 pH meter. Furthermore, the influence of catalyst dosage was explored to determine the optimal amount for efficient H_2O_2 production. Reusability assessments were performed over multiple cycles, in which 50 mg of the catalyst was recovered by centrifugation, washed thoroughly, and dried before reuse.

2.8. Evaluation of electrochemical properties

The electrochemical behavior of the synthesized materials was evaluated using a CS310M electrochemical workstation in a conventional three-electrode configuration. The system consisted of a glassy carbon electrode (GCE) as the working electrode, a platinum wire as the counter electrode, and a saturated calomel electrode (SCE) as the reference electrode. Phosphate-buffered saline (PBS) solution served as the electrolyte medium throughout the measurements. For electrode fabrication, 5 mg of the photocatalyst was dispersed in 1 mL of absolute ethanol and sonicated for 30 minutes to ensure homogeneous dispersion. About 5 μL of the resulting suspension was first drop-cast onto the GCE surface and dried under ambient conditions, then 5 μL of a Nafion® solution was drop-cast and allowed to dry under ambient conditions prior to use. Electrochemical properties were investigated through a combination of techniques, including electrochemical impedance spectroscopy (EIS), Mott–Schottky analysis, and photocurrent response measurements, to assess charge transport characteristics as well as interfacial charge separation efficiency.

2.9. Density functional theory calculations

Density functional theory calculations were conducted using the SIESTA package. The valence electrons were represented using a double-zeta basis set with polarization functions (DZP). For Brillouin zone sampling, a Monkhorst–Pack *k*-point grid of $3 \times 3 \times 3$ was employed. The real-space grid used for numerical integration corresponded to a mesh cutoff energy of 200 Ry, which was found to be sufficient to ensure total energy convergence. Atomic structures were optimized by minimizing the Hellmann–Feynman forces to below 0.04 eV Å^{-1}, and electronic convergence was achieved when the change in the density matrix fell below 10^{-4} eV between SCF cycles. Periodic boundary conditions were applied in all three spatial directions for bulk calculations. For surface models, periodicity was maintained in the *x* and *y* directions, while a vacuum layer of 40 Å was introduced along the *z*-axis to avoid artificial interactions between repeated slabs. In all cases, full structural relaxation was performed. To gain deeper insight into the bonding characteristics within the EuCN composite, the redistribution of electronic charge was examined through charge density difference analysis with respect to isolated atoms. This calculation was performed using the Denchar module integrated in the SIESTA software package. The charge density difference ($\Delta\rho$) was computed using eqn (2).

$$\Delta\rho = \rho_{\mathrm{EuCN}} - \sum_i \rho_{\mathrm{isolated},i} \tag{2}$$

where ρ_{EuCN} represents the total charge density of the composite system, and $\rho_{\mathrm{isolated},i}$ denotes the charge density of each constituent atom (Eu, O, or N) in its non-interacting state, calculated under identical computational conditions. To enhance the clarity of the charge redistribution patterns, isosurface values of 0.020022 and 0.0090022 e Å^{-3} were applied for the relaxed and fixed CN configurations, respectively.

The work function was obtained as the difference between the vacuum electrostatic potential and the Fermi energy. The vacuum level was obtained by averaging the macroscopic Hartree potential in the flat vacuum region, excluding boundary artifacts near the cell edges.

3. Results and discussion

3.1. Characteristics of materials

HPLC results for the extract are shown in Fig. S6. In Fig. S6b, two dominant peaks corresponding to quercetin and kaempferol are observed, indicating that the extract is rich in polyphenolic compounds. These flavonoids contain multiple phenolic –OH groups, which can coordinate with Eu^{3+} ions through oxygen donor atoms. During synthesis, such coordination promotes the formation of a homogeneous Eu-organic intermediate network, thereby regulating nucleation and suppressing localized aggregation of Eu species. Upon subsequent thermal treatment, this controlled nucleation pathway facilitates a more uniform dispersion of Eu_2O_3 particles within the carbon matrix derived from the extract. In addition, the polyphenolic compounds can adsorb on the particle surface and act as stabilizing agents, limiting particle growth and coalescence. The chromatogram recorded at 245 nm (Fig. S6d) indicates the presence of other minor constituents, whereas vitamin C is absent or present at a negligible level under the present analytical conditions. Therefore, the improved distribution of Eu_2O_3 is primarily attributed to the polyphenol-rich fraction of the green extract.

As shown in Fig. 1a, the FTIR spectra reveal the characteristic vibrational features of CN, Eu_2O_3, and EuCN composites. The broad absorption band observed in the region of 3000–3500 cm^{-1} is attributed to the N–H stretching vibrations, indicative of surface –NH or $-NH_2$ groups.[28] The absorption features appearing between 1200 and 1750 cm^{-1} correspond to characteristic stretching vibrations of σ- and π-bonds associated with the C–N framework.[28] Notably, the peak centered at 1643 cm^{-1} is assigned to the C=N stretching mode, whereas the signals at 1235, 1321, and 1403 cm^{-1} can be ascribed to various C–N single bond vibrations.[28] Furthermore, the two sharp bands located at 809 and 893 cm^{-1} are characteristic of the out-of-plane bending vibrations of *s*-triazine rings, which are typical structural motifs in carbon nitride networks.[28] The FTIR spectrum of Eu_2O_3 displays a characteristic peak at 632 cm^{-1}, which can be ascribed to Eu–O stretching vibrations.[29] Additionally, a broad absorption band around 3430 cm^{-1} corresponds to surface-adsorbed or hydrated water molecules.[29] Notably, other regions of the FTIR spectrum of Eu_2O_3 may vary depending on the nature of the solvent or reducing agent used during synthesis, aligning well with observations reported in our earlier studies. The FTIR spectra of the EuCN composites clearly exhibit characteristic bands attributable to both CN and Eu_2O_3, confirming the effective integration of these components within the hybrid material. Fig. 1b presents the XRD patterns of pristine CN, pure Eu_2O_3, and EuCN composites with varying Eu_2O_3 contents. The CN sample displays two characteristic diffraction peaks at 2θ = 13.08 and 27.72°, corresponding to the (100) and (002) crystal planes, respectively.[30] These reflections are typical of the in-plane structural packing and interlayer stacking of CN, confirming its layered structure. In contrast, the XRD pattern of Eu_2O_3 exhibits sharp and intense peaks at 28.81, 30.58, 47.72, and 55.53° which are indexed to the (222), (400), (440), and (622) planes of its cubic phase structure.[29] As the Eu_2O_3 content increases in the EuCN composites, the intensity and resolution of Eu_2O_3 related peaks become more prominent, indicating improved crystallinity and greater loading of Eu_2O_3 particles on the CN matrix. Importantly, the characteristic peaks of CN remain unaltered in position and intensity, suggesting that the incorporation of Eu_2O_3 does not disrupt the intrinsic framework of CN. These results collectively demonstrate that Eu_2O_3 is well-dispersed within the composites while retaining its distinct crystalline identity, pointing toward a physical interaction between the two components rather than the formation of a new compound phase.

Nitrogen adsorption–desorption isotherms and pore size distribution curves of the samples are presented in Fig. 1c and d, respectively. All samples exhibit type IV isotherms with distinct H3-type hysteresis loops at high relative pressures, which are characteristic of mesoporous materials with slit-like pores formed by the aggregation of plate-like particles. The corresponding BET data summarized in Table 1 show that pristine CN possesses the highest specific surface area of 54.280 m^2 g^{-1} and a relatively large pore volume of 0.125 cc g^{-1}, along with an average pore diameter of 37.909 Å. Upon decoration with Eu_2O_3, all EuCN composites exhibit a gradual decrease in the surface area and pore volume, suggesting that Eu_2O_3 particles partially occupy or block the pore channels of CN. Among the composites, 5EuCN exhibits the largest average pore diameter (281.124 Å), indicating the formation of wider

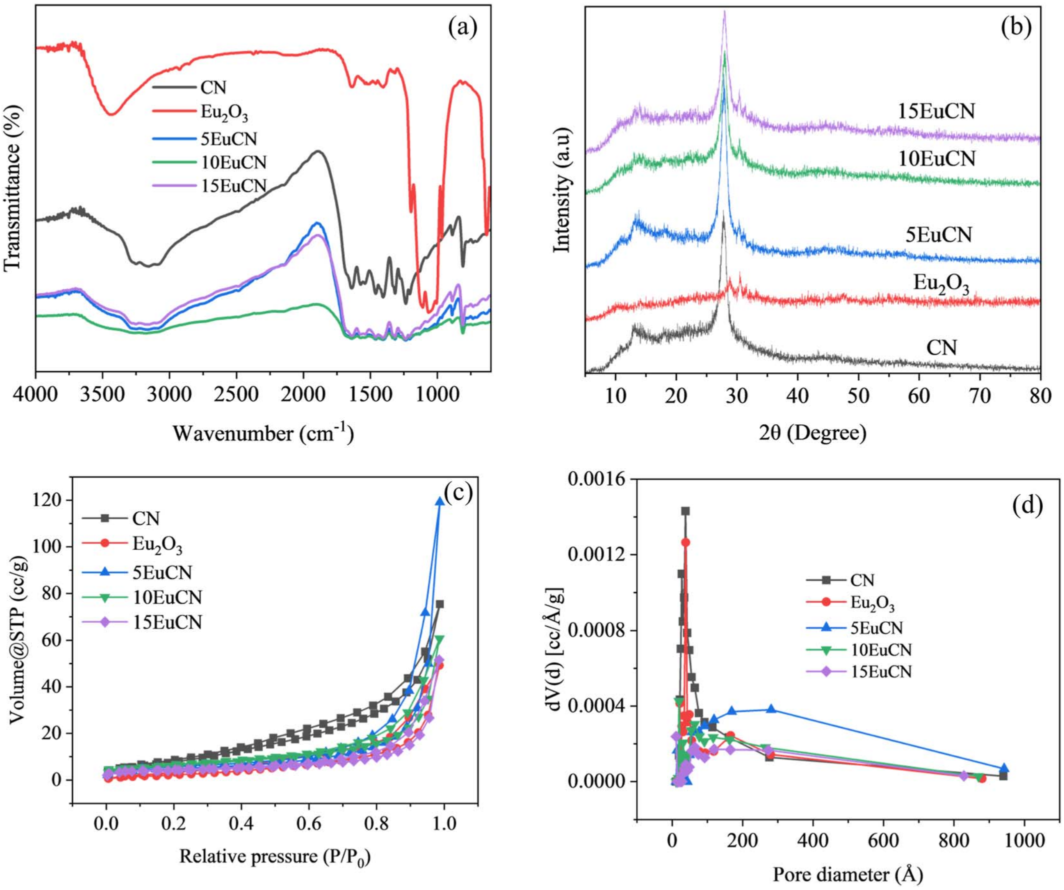

Fig. 1 (a) FTIR spectra, (b) XRD patterns, (c) N_2 adsorption–desorption spectra, and (d) pore size distribution of CN, Eu_2O_3, 5EuCN, 10EuCN, and 15EuCN.

Table 1 BET surface area, pore diameter, and pore volume of CN, Eu_2O_3, and EuCN composites

Materials	Surface area (m^2 g^{-1})	Pore size (Å)	Pore volume (cc g^{-1})
CN	54.280	0.125	37.909
Eu_2O_3	29.749	0.083	38.334
5EuCN	30.784	0.190	281.124
10EuCN	25.330	0.094	19.686
15EuCN	18.714	0.081	11.154

mesopores or partial exfoliation of CN layers due to moderate Eu_2O_3 incorporation. However, further increasing the Eu_2O_3 content leads to a sharp decline in both pore diameter and surface area. In particular, 15EuCN shows the lowest values (18.714 m^2 g^{-1} and 11.154 Å) implying that excess Eu_2O_3 causes significant pore narrowing or structural compaction. Notably, the 10EuCN sample exhibits a well-balanced porous structure, with a moderate surface area (25.330 m^2 g^{-1}), pore volume (0.094 cc g^{-1}), and average pore size (19.686 Å). In addition, its narrow pore size distribution (Fig. 1d) reflects good structural uniformity. These results indicate that a medium Eu_2O_3 content is favorable for maintaining the mesoporous framework of CN while preventing aggregation or excessive pore blockage.

Fig. 2 provides insight into the morphology and surface characteristics of Eu_2O_3, CN, and the 10EuCN composite. The Eu_2O_3 sample consists of nanoparticles with sizes below 500 nm, which tend to aggregate, possibly due to incomplete crystal growth or the high surface energy of individual particles. In contrast, CN exhibits a layered morphology composed of thin sheets that naturally stack and form dense agglomerates. In the case of the 10EuCN composite, Eu_2O_3 particles are clearly observed to be uniformly anchored on the surface of CN sheets, indicating a successful combination of the two components and suggesting good interfacial contact that may facilitate charge separation and transfer. Elemental mapping and the corresponding EDX spectra (Fig. 2e and h) reveal a uniform distribution of C, N, Eu, and O across the material's surface, thus confirming the successful incorporation of Eu_2O_3 on CN. The TEM images (Fig. 2f and g) clearly demonstrate that Eu_2O_3 nanoparticles are uniformly distributed on the surface of CN, exhibiting good dispersion and limited aggregation, with particle sizes below 200 nm. This well-dispersed morphology suggests that the adopted synthesis method effectively prevents particle agglomeration. Furthermore, the SAED pattern in Fig. 2i displays distinct diffraction rings, from which the lattice spacing was calculated to be approximately 0.2917 nm. This value is consistent with the (400) crystallographic plane of cubic

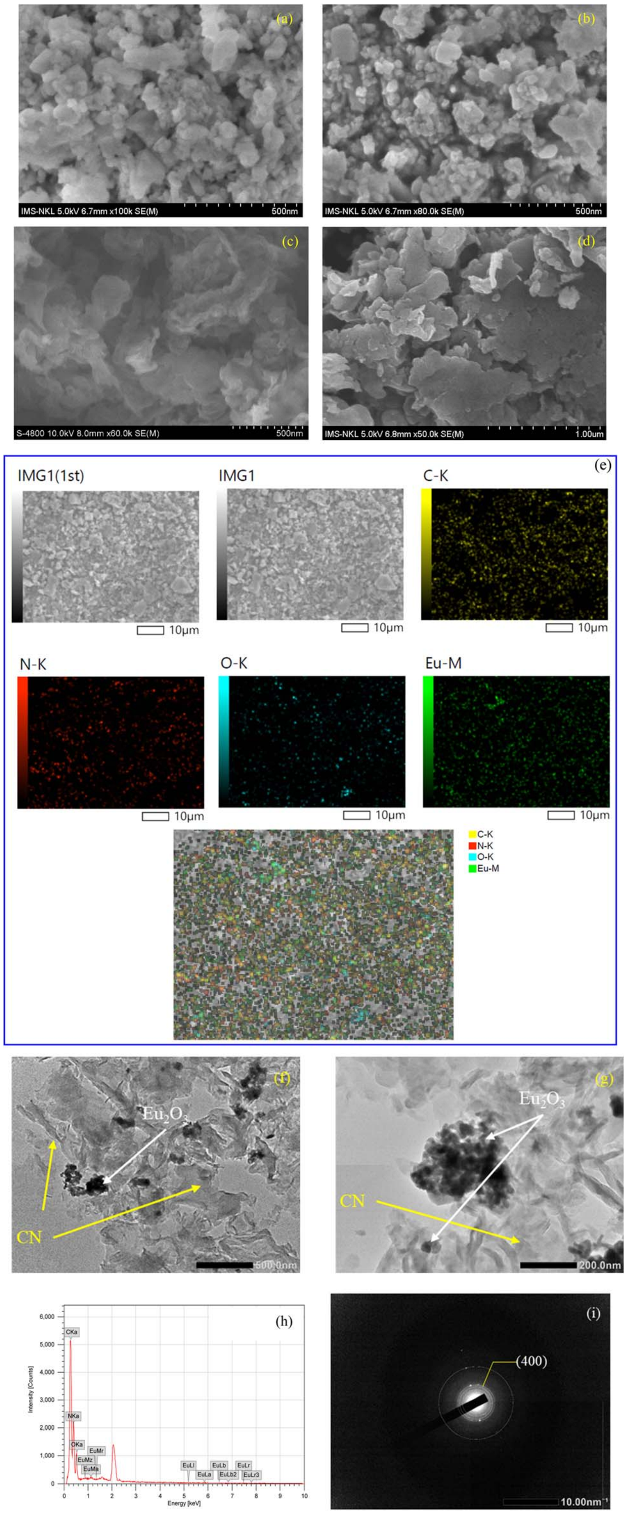

Fig. 2 FE-SEM images of (a) and (b) Eu_2O_3, (c) CN, and (d) 10EuCN composite; (e) elemental mapping, (f and g) TEM images, (h) EDX spectra, and (i) SAED image of the 10EuCN composite.

Eu_2O_3, and closely matches the interplanar distance of 0.2920 nm obtained by XRD.

Fig. 3 presents the XPS spectra of the EuCN composite. The survey spectrum (Fig. 3a) exhibits only Eu, O, C, and N signals, confirming the absence of detectable impurities and the high purity of the material. In the high-resolution C 1s spectrum (Fig. 3b), deconvolution yields peaks at 284.63 eV (sp^2 C=C), 288.01 eV (N–C=N within the heterocycle), and 293.32 eV (π–π^* transitions of the aromatic CN framework).[31] The N 1s spectrum (Fig. 3c) features peaks at 398.54 eV (sp^2 C–N=C), 400.46 eV (tertiary N in the triazine ring), and 404.16 eV ($-NH_2$ surface groups).[31] The dominant sp^2 C–N=C peak confirms the conjugated CN framework, while the tertiary N signal verifies the integrity of the heptazine structure.[32] In the O 1s region (Fig. 3d), the bands at 531.27 and 532.62 eV are assigned to adsorbed water and Eu–O bonds, respectively.[33] The Eu 3d spectrum (Fig. 3e) confirms the co-existence of Eu^{3+} and Eu^{2+} oxidation states. For the Eu $3d_{3/2}$ level, the peaks at 1165.98 eV (Eu^{3+}) and 1157.01 eV (satellite peak for Eu^{2+}) are observed, while the Eu $3d_{5/2}$ level displays peaks at 1136.75 eV (Eu^{3+}) and 1127.18 eV (satellite for Eu^{2+}).[34] Furthermore, the deconvoluted Eu 4d spectrum (Fig. 3f) exhibits two major peaks at 137.58 and 143.37 eV, which are attributed to the multiplet splitting of the $4d$–$4f^6$ configurations of Eu^{3+}.[34] These results demonstrate successful incorporation of Eu_2O_3 into the CN matrix and the coexistence of Eu^{2+}/Eu^{3+} redox couples, a feature that may enhance interfacial charge separation and promote photocatalytic performance.

3.2. Photocatalytic performance

3.2.1. Photodegradation efficiency of MB. Fig. 4a compares the visible-light-driven degradation of MB over pristine CN, Eu_2O_3, and EuCN composites. After 90 minutes of illumination, CN and Eu_2O_3 achieve only 24.57 and 28.77% MB removal, respectively, reflecting rapid recombination of photogenerated charge carriers and limited charge transport. Incorporation of Eu_2O_3 into CN markedly enhances performance, and the 5EuCN and 10EuCN samples reach 81.78 and 93.82% degradation, respectively. This improvement arises from synergistic interactions between CN and Eu_2O_3, which broaden light absorption, promote charge separation, and accelerate the formation of reactive oxygen species. When the Eu_2O_3 content is increased further to produce 15EuCN, the degradation efficiency falls to 67.36%. This can be explained by the fact that the excessive Eu_2O_3 loading blocks active sites on CN, diminishes light penetration, and hinders access of reactants to catalytic centers.

The photocatalytic degradation kinetics of MB over the prepared samples were evaluated using a pseudo-first-order kinetic model, as illustrated in Fig. 4b. Pristine CN and Eu_2O_3 exhibited relatively low rate constants of 0.00265 and 0.00257 min^{-1}, respectively, which can be attributed to inefficient charge carrier separation and limited generation of reactive species. Upon coupling Eu_2O_3 with CN, a substantial enhancement in the reaction kinetics was observed. Specifically, the k values increased to 0.01521 and 0.02188 min^{-1} for the 5EuCN and 10EuCN composites, respectively, indicating a significant improvement in photocatalytic activity due to the synergistic effects between CN and Eu_2O_3. However, further increasing the Eu_2O_3 content to 15 wt% led to a decline in the rate constant to 0.00915 min^{-1}. This reduction is likely

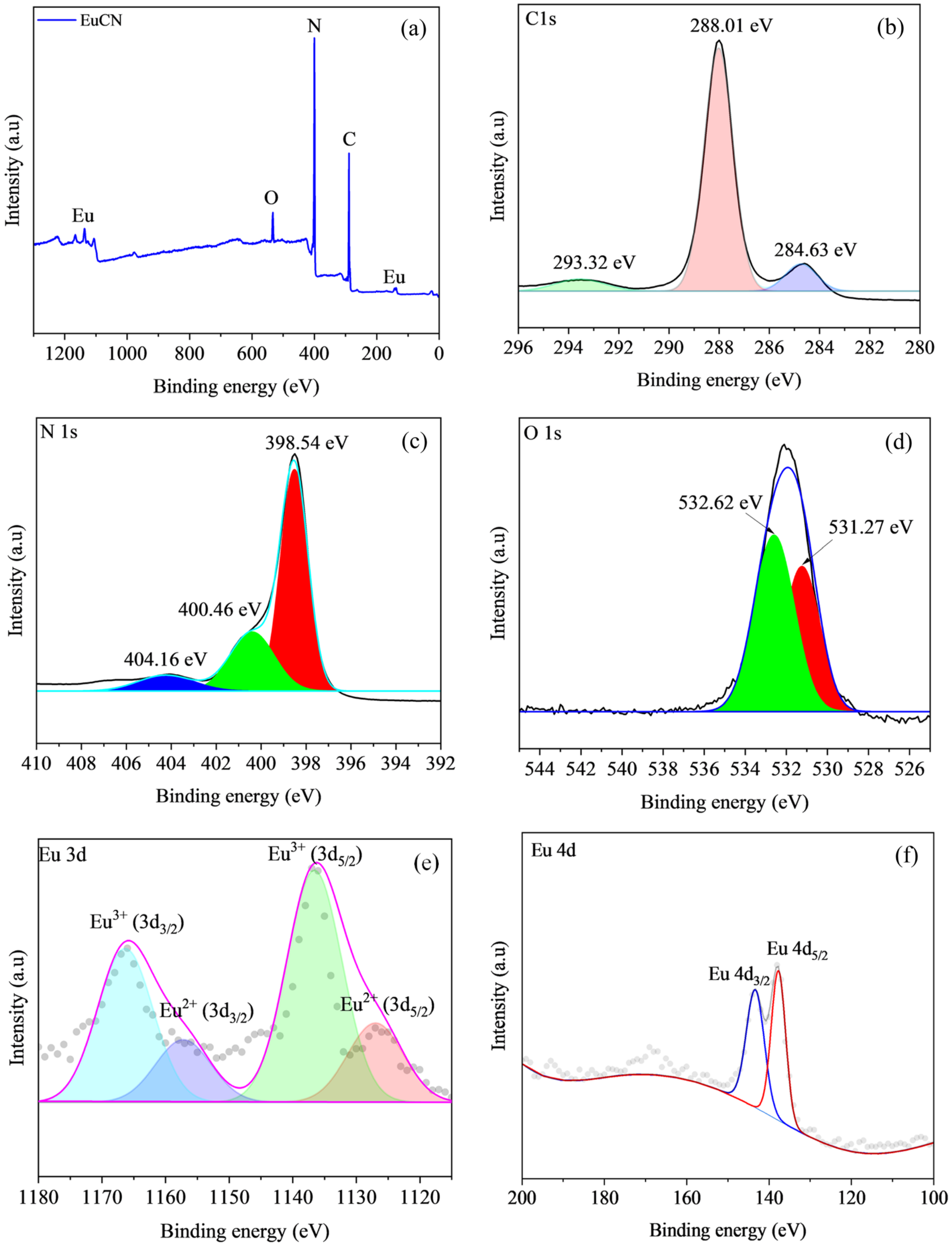

Fig. 3 (a) Full XPS survey spectrum; high-resolution spectra of (b) C 1s, (c) N 1s, (d) O 1s, (e) Eu 3d, and (f) Eu 4d of the 10EuCN composite.

associated with excessive Eu_2O_3 coverage, which may hinder light absorption and obstruct active sites on the CN surface.[35]

In addition, the effects of operational parameters such as catalyst dosage, pollutant concentration, and solution pH were investigated. As shown in Fig. 4c, increasing the catalyst dosage led to a gradual enhancement in MB photodegradation efficiency.[36] This improvement can be attributed to the increased availability of the active surface area and adsorption sites, which facilitate greater interaction between the photocatalyst and the target pollutant.[36] The increase in adsorption capacity is particularly evident under dark conditions, where higher catalyst amounts show stronger adsorption of MB. However, the optimal catalyst dosage was determined to be 30 mg. Although higher dosages of 40 and 50 mg achieved slightly higher degradation efficiencies (94.72 and 93.45%, respectively) compared to 30 mg (93.82%), the marginal gain in performance does not justify the additional material cost, making 30 mg the most efficient and economical choice for photocatalytic

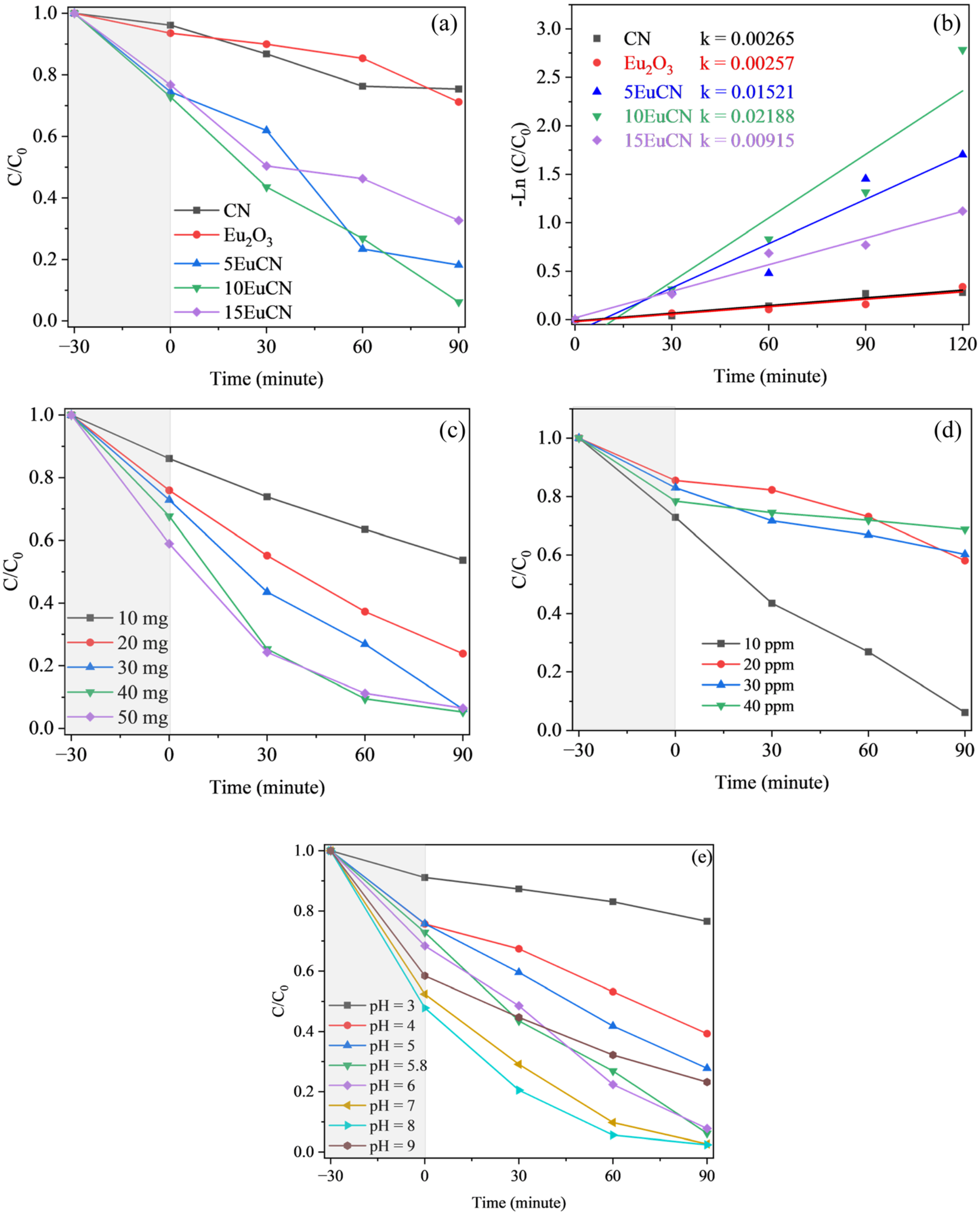

Fig. 4 (a) Photodegradation efficiency and (b) pseudo-first-order kinetic plots for the degradation of methylene blue over Eu_2O_3, CN, and EuCN composites under visible light irradiation; effect of (c) different masses of the photocatalyst, (d) different concentrations of MB, and (e) different pH on the photodegradation efficiency of MB of the material.

application. Fig. 4d illustrates the effect of initial pollutant concentration on the photocatalytic degradation efficiency of MB. A clear decline in degradation performance is observed as the concentration increases.[37] Specifically, the efficiency drops from 93.82% at 10 ppm to 41.88, 39.75, and 31.25% corresponding to the concentrations of 20, 30, and 40 ppm, respectively. This trend can be explained by the fact that, at higher dye concentrations, the solution becomes more intensely colored, which reduces light penetration and limits the activation of the photocatalyst.[38] Furthermore, the excessive number of dye molecules may saturate or block the active sites on the catalyst surface, thereby hindering the generation and interaction of reactive species necessary for efficient photodegradation.[39] Despite the reduction in efficiency, it is noteworthy that even at concentrations three to four times higher than the lowest tested level, the decrease in performance is only two- to threefold. This indicates that the EuCN composites retain considerable photocatalytic activity across a broad concentration range. Such stability under high pollutant loads demonstrates the material's potential applicability in real wastewater treatment systems, where contaminant concentrations are often variable and significantly higher than those under laboratory conditions.

The influence of solution pH on the photocatalytic performance of the EuCN composites was also investigated. As depicted in Fig. 4e, the photocatalytic efficiency generally increases with rising pH, reaching a maximum at pH 8 but subsequently declines at pH 9. This behavior can be attributed to the surface charge dynamics of the CN-based photocatalyst. Under acidic conditions, the $-NH_2$ and nitrogen-containing groups on the CN framework tend to become protonated, leading to a positively charged surface.[40] This weakens the electrostatic interaction with the cationic MB dye, thereby reducing its adsorption and, consequently, the overall photocatalytic activity. Conversely, in strongly alkaline environments (pH 9), although the catalyst surface becomes negatively charged, which theoretically favors the adsorption of cationic dyes like MB, an excessive amount of OH^- in solution competes with MB for adsorption sites.[41] This electrostatic competition reduces the effective interaction between MB and the photocatalyst surface, resulting in lower degradation efficiency. The recyclability and structural stability of the EuCN composites were evaluated to assess their practical applicability in photocatalytic processes. As shown in Fig. 5a, the material retained a photodegradation efficiency of 67.34% after six consecutive cycles, demonstrating good stability and reusability under repeated visible-light irradiation. Furthermore, the XRD patterns before and after the recycling tests (Fig. 5b) exhibit negligible changes, with no significant shift or disappearance of characteristic diffraction peaks. The FTIR spectra (Fig. 5c) further confirm the structural stability of the material. Notably, an increase in the broad absorption band in the region of 3000 to 3500 cm^{-1} is observed after cycling, which may be attributed to the accumulation of intermediate species or surface hydroxyl groups. This indicates that the crystalline structure of the EuCN composites remains largely intact after photocatalytic operation.

3.2.2. Evaluation of H_2O_2. The photocatalytic performance of CN, Eu_2O_3, and EuCN composites for H_2O_2 generation under UV irradiation is presented in Fig. 6a. Pristine CN and Eu_2O_3 exhibited limited photocatalytic activity, producing relatively low H_2O_2 concentrations of 91.13 and 100.96 μM, respectively. This modest performance is likely due to poor light utilization and rapid recombination of photogenerated electron–hole pairs, which restrict the formation of reactive oxygen species. In contrast, the incorporation of Eu_2O_3 into the CN matrix led to a remarkable improvement in H_2O_2 production. The EuCN composites with increasing Eu_2O_3 loading (5, 10, and 15%) achieved H_2O_2 concentrations of 115.47, 233.73, and 121.71 μM, respectively. Among the tested samples, the 10EuCN composite exhibited the highest H_2O_2 yield, indicating an optimal balance between charge carrier separation and the availability of active sites. The improved performance is attributed to the synergistic

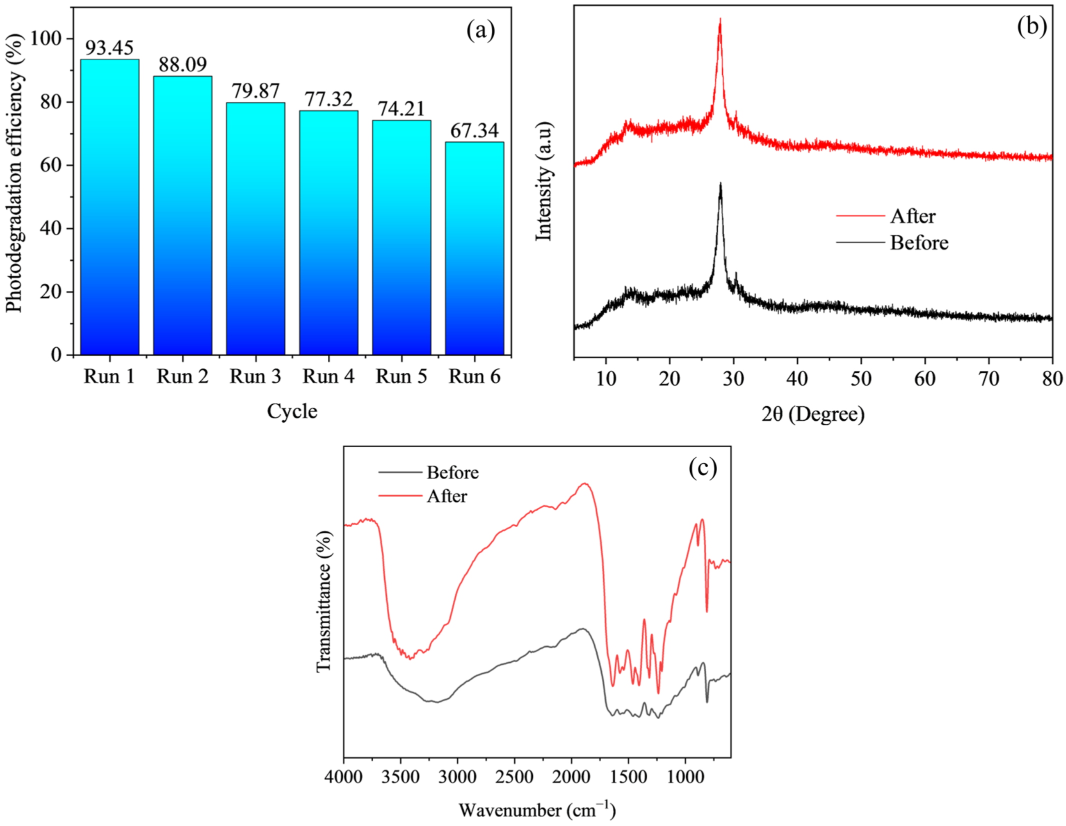

Fig. 5 (a) Recyclability of the EuCN composites for the photodegradation of methylene blue using 50 mg of the catalyst, (b) XRD patterns, and (c) FTIR spectra of the material before and after the recycling process.

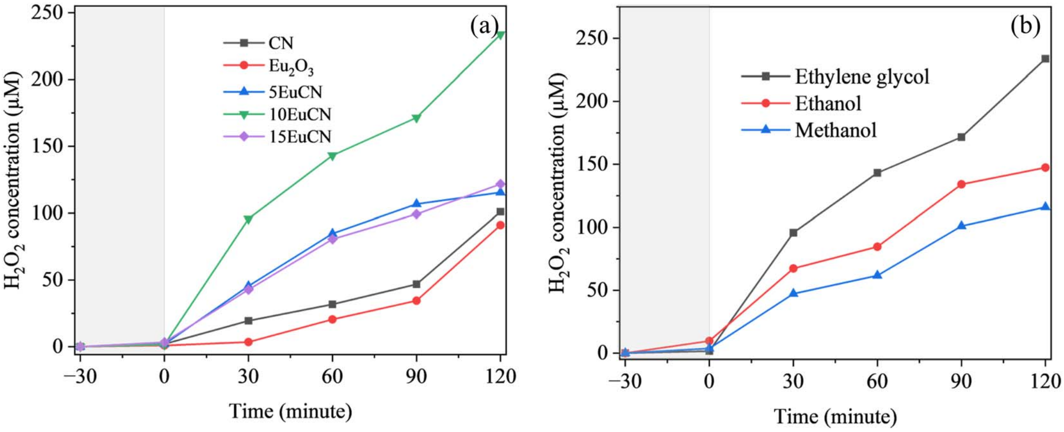

Fig. 6 (a) Photocatalytic production and (b) photocatalytic generation rate of H_2O_2 by CN, Eu_2O_3, and EuCN composites.

interaction between Eu_2O_3 and CN, which enhances charge migration, suppresses recombination, and promotes the two-electron oxygen reduction pathway necessary for H_2O_2 formation. However, a further increase in Eu_2O_3 content to 15% resulted in a notable decrease in H_2O_2 generation. This decline can be explained by the excessive coverage of the CN surface with Eu_2O_3 nanoparticles, which may block light absorption sites and passivate surface defects that are critical for photocatalytic activity.[42] Additionally, the excess Eu_2O_3 may introduce recombination centers or limit the mobility of photogenerated carriers, thereby reducing overall photocatalytic efficiency.

In addition, the effect of sacrificial agents on H_2O_2 generation was investigated (Fig. 6b). Among the tested electron donors, ethylene glycol exhibited the highest H_2O_2 production (233.73 μM), followed by ethanol (147.36 μM) and methanol (115.91 μM). The superior performance of ethylene glycol is likely due to its strong electron-donating ability and efficient interaction with the photocatalyst. The observed trend in H_2O_2 generation efficiency can be correlated with the structural and electronic properties of the sacrificial agents, which influence their ability to donate electrons and suppress charge recombination during the photocatalytic process.[43]

The influence of catalyst dosage on the efficiency of H_2O_2 generation was also systematically investigated, as illustrated in Fig. 7a. As the amount of the EuCN catalyst increased from 5 mg to 10 mg, the H_2O_2 yield initially improved, reaching a maximum of 233.73 μM at 10 mg, followed by a gradual decline to 228.96, 216.05, and 142.57 μM corresponding to catalyst dosages of 20, 30, and 40 mg, respectively. This decrease at higher dosages can be attributed to the light-scattering effect and increased turbidity in the suspension, which reduces light penetration and subsequently limits the activation of the photocatalyst.[44] Interestingly, a deviation from this declining trend was observed at 50 mg, where the H_2O_2 generation unexpectedly rose to 299.39 μM. This anomalous enhancement may be attributed to improved catalyst dispersion and a more favorable spatial arrangement of the photocatalyst particles.[45] At this higher loading, the catalyst may form a more loosely packed layer with increased surface exposure, allowing better light absorption and facilitating the diffusion of O_2 molecules into the active reaction sites.[46] Additionally, the denser presence of active species might contribute to partial suppression of H_2O_2 decomposition by stabilizing the product through mild adsorption, thereby improving its accumulation over time.

The influence of solution pH on the photocatalytic production of H_2O_2 was further examined, as shown in Fig. 7b. In contrast to the trend observed in MB photodegradation, lower pH values were found to enhance H_2O_2 generation, with the highest yield recorded at pH 4. This improvement under mildly acidic conditions can be attributed to the increased concentration of H^+ ions, which facilitate effective charge separation by suppressing electron–hole recombination.[47] As a result, more photogenerated electrons are available to participate in the reduction of molecular oxygen, promoting the formation of H_2O_2. However, a further decrease in pH to 3 led to a noticeable decline in H_2O_2 production. This reduction may be due to the excessive presence of protons, which competitively consume electrons during oxygen reduction reactions. Such interference reduces the likelihood of $^{\bullet}O_2^-$ formation making H_2O_2 generation lower.[48]

The reusability and structural stability of the EuCN composites for photoproduction of H_2O_2 were also evaluated over six consecutive cycles, as presented in Fig. 7c. The results demonstrate that the EuCN photocatalyst retains considerable photocatalytic activity, achieving an H_2O_2 yield of 205.91 μM after the sixth cycle. This level of retention reflects strong catalytic durability, comparable to its performance in methylene blue degradation and highlights the material's robustness under repeated operational conditions. The minimal loss in efficiency suggests that the active sites remain accessible and the interfacial charge transfer properties are largely preserved throughout the reuse cycles. Moreover, the XRD patterns and FTIR spectra recorded before and after the recyclability test (Fig. 7d and e) exhibit no significant changes in the peak position or intensity, confirming the structural integrity of the EuCN composite. The absence of new crystalline phases or peak broadening indicates that the photocatalyst resists photocorrosion and does not undergo phase transformation during

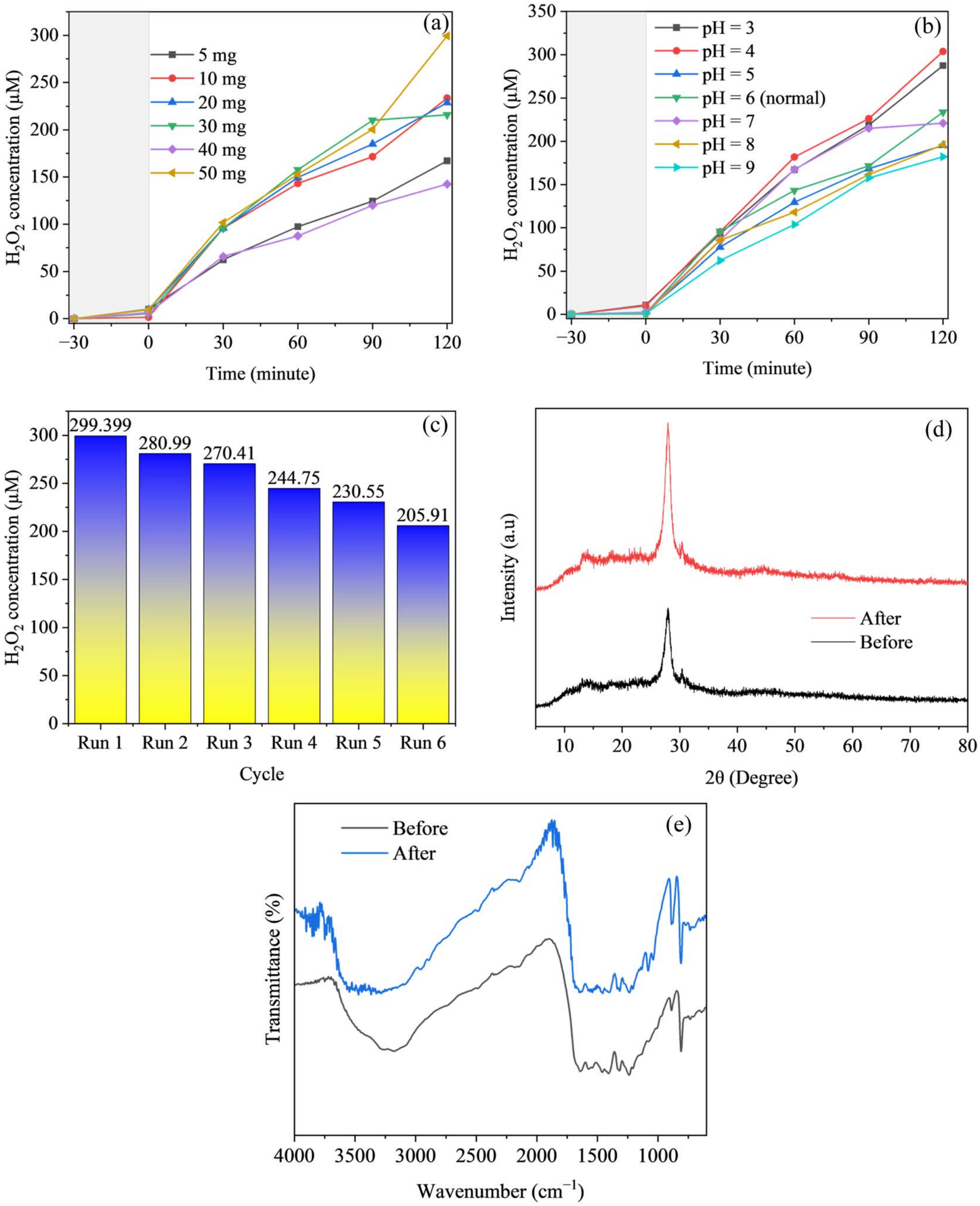

Fig. 7 Effects of (a) catalyst dosage and (b) pH on H_2O_2 photoproduction; (c) recyclability of EuCN composites over six cycles using 50 mg of the catalyst, (d) XRD patterns, and (e) FTIR spectra before and after recycling.

repeated UV irradiation and exposure to reactive species. Additionally, EuCN demonstrates a competitive performance in photocatalysis compared to related materials, as shown in Table 2.

3.3. DFT results and the photocatalyst mechanism

The photoelectrochemical and optical properties of CN, Eu_2O_3, and EuCN composites were further examined to elucidate the role of Eu_2O_3 incorporation in enhancing photocatalytic performance, as shown in Fig. 8. The Nyquist plots (Fig. 8b) indicate that 10EuCN exhibits a larger arc radius than pristine CN, suggesting an increased interfacial charge-transfer resistance. However, this increase does not necessarily imply inferior performance. In S-scheme heterojunction systems, the formation of an internal electric field and interfacial band bending can regulate carrier migration behavior, in which selective recombination and directional charge transfer are essential for preserving strong redox capability.[53] The incorporation of Eu^{3+} introduces localized 4f electronic states into the CN matrix, which can act as efficient electron trapping centers.[54] These sites can capture photogenerated electrons, delaying their recombination with holes and thereby prolonging carrier

Table 2 Performance comparison with other photocatalysts for H_2O_2 photoproduction

No	Materials	Applications	Efficiency	Ref.
1	Ti_3C_2/porous g-C_3N_4	H_2O_2 photoproduction	131.71 μmol g^{-1} h^{-1}	49
2	g-C_3N_4/PDI	H_2O_2 photoproduction	21.08 μmol g^{-1} h^{-1}	50
3	Sm-Fe doped $LaNiO_3$/g-C_3N_4	MB photodegradation	0.0175 min^{-1}	51
4	CeO_2-C-g-C_3N_4	MB photodegradation	0.01936 min^{-1}	52
5	EuCN composite	H_2O_2 photoproduction	11686.5 μM g^{-1} h^{-1}	This work
		MB photodegradation	0.02188 min^{-1}	

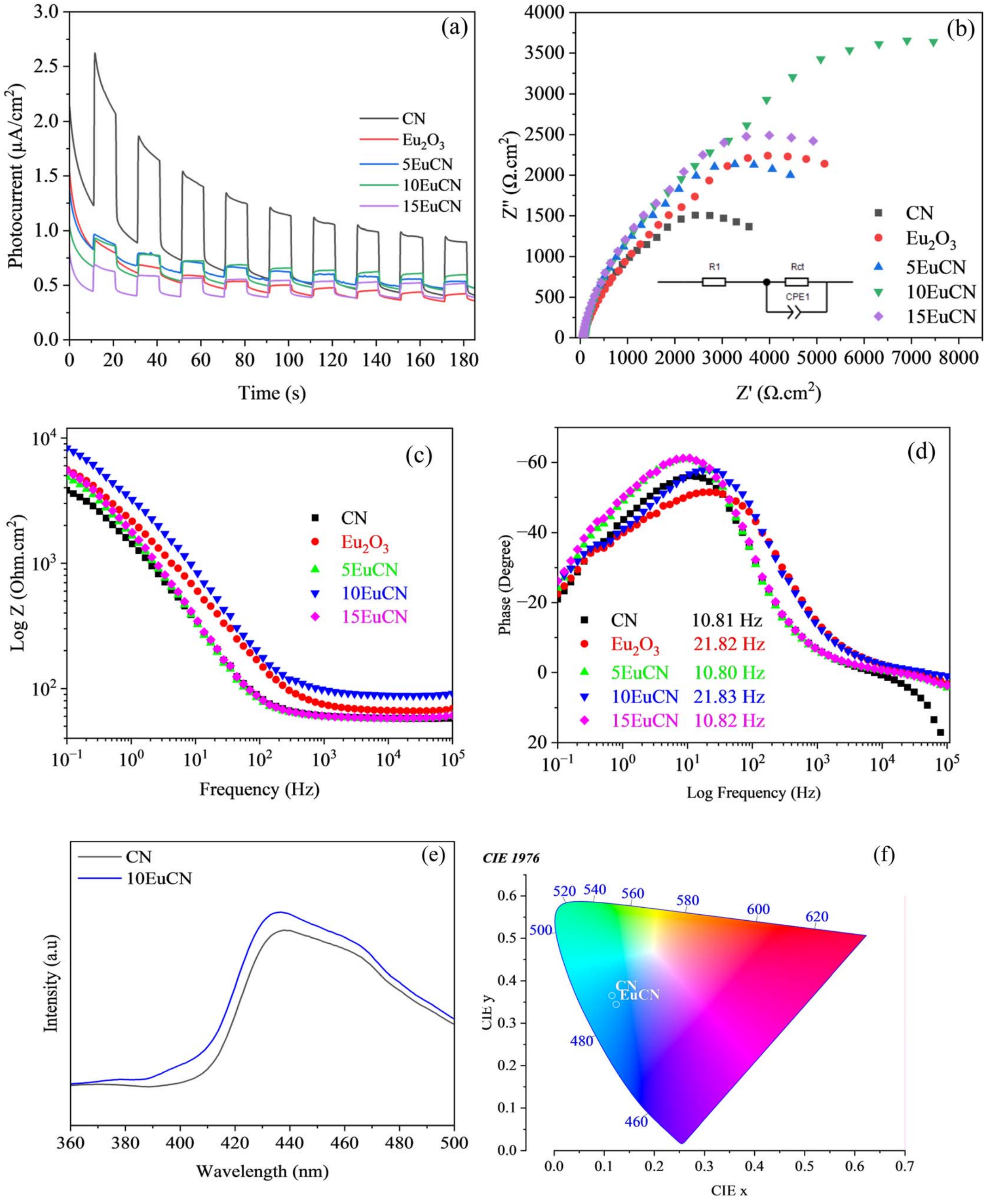

Fig. 8 (a) Transient photocurrent responses, (b) EIS spectra, (c) Bode magnitude plots, and (d) Bode phase plots of CN, Eu_2O_3, and EuCN composites; (e) PL intensity and (f) CIE plot of CN and the 10EuCN composite.

Table 3 R_s, R_{ct}, CPE-T, and CPE-P values of materials from EIS fitting

Samples	R_s (Ω cm^2)	R_{ct} (Ω cm^2)	CPE-T (F g^{-1})	CPE-P (F g^{-1})
CN	56.84	4162.2	1.35×10^{-4}	7.66×10^{-1}
Eu_2O_3	63.13	6746.6	9.99×10^{-5}	6.9×10^{-1}
5EuCN	56.91	5462.7	1.15×10^{-4}	8.03×10^{-1}
10EuCN	84.29	9527	6.12×10^{-5}	7.29×10^{-1}
15EuCN	57.07	6359.9	1.11×10^{-4}	7.97×10^{-1}

lifetimes.[55] This mechanism is corroborated by the transient photocurrent response in Fig. 8a, where 10EuCN demonstrates a more stable and sustained photocurrent under repeated light on–off cycles, despite its slightly lower initial intensity compared to CN. The more stable photocurrent indicates effective suppression of rapid recombination and prolonged participation of electrons in surface redox reactions.

The electrochemical parameters extracted from EIS fitting (Table 3) further support this conclusion. The solution resistance (R_s) of 10EuCN slightly increases from 56.84 to 84.29 Ω cm^2 due to interfacial changes introduced by Eu_2O_3 deposition. More significantly, the polarization resistance (R_{ct}) increases markedly from 4162.2 to 9527 Ω cm^2, indicating a greater charge storage capability and stronger interfacial polarization effect. While a higher R_{ct} often implies slower interfacial charge transfer, in this case it reflects enhanced charge accumulation due to trapping. This interpretation is supported by the lower constant phase element time constant (CPE-T), which drops from 1.35×10^{-4} F g^{-1} (CN) to 6.12×10^{-5} F g^{-1} (10EuCN). A lower CPE-T indicates reduced capacitive behavior, possibly resulting from localized electron trapping and restricted ion mobility. Meanwhile, the CPE-P values remain in the range of 0.73–0.81, suggesting that all samples exhibit stable, though non-ideal, capacitive behavior.

Based on the Nyquist and transient photocurrent results, the Bode magnitude and phase plots in Fig. 8c and d confirm the advantages of Eu_2O_3 decoration on CN. As shown in Fig. 8c, at 0.1 Hz pristine CN exhibits a $|Z|$ of 3.82×10^3 Ω cm^2, whereas 10EuCN reaches 8.31×10^3 Ω cm^2, which reflects greatly enhanced interfacial capacitance due to Eu^{3+} related 4f trap levels capturing photogenerated electrons and delaying recombination. The 5EuCN, 15EuCN, and Eu_2O_3 samples show more modest increases of 27.6 to 46.4%, indicating that 10 wt% is the optimal loading for trap-mediated charge storage. In the phase plot (Fig. 8f), CN reaches its minimum phase of $-56.1°$ at 10.81 Hz ($\tau = 14.7$ ms), while 10EuCN shifts to $-57.9°$ at 21.83 Hz ($\tau = 7.3$ ms). This twofold reduction in carrier lifetime shows that once Eu_2O_3 trap sites are filled, the electrons are released into the external circuit more rapidly. Combining the high low-frequency impedance in Fig. 8c with the accelerated charge-transfer kinetics in Figure 8d, 10EuCN achieves both prolonged carrier separation and swift electron delivery, which together underpin its superior photocatalytic performance. Further evidence supporting the beneficial role of Eu^{3+} can be seen in the PL spectra (Fig. 8e). The 10EuCN sample shows a slight enhancement in the PL intensity compared to CN, which is attributed to radiative transitions originating from Eu-related emission centers rather than increased recombination. The partially allowed 4f–4f transitions of Eu^{3+}, influenced by symmetry breaking and ligand-field effects in the CN framework, contribute to this luminescence.[56] The chromaticity coordinates shown in the CIE 1976 diagram (Fig. 8f) also shift slightly upon Eu incorporation, indicating modified optical emission behavior. These changes suggest that Eu^{3+} not only alters the electronic structure but also broadens the light-harvesting capability of the composite.[57] The combined effects of improved charge carrier dynamics and enhanced optical utilization collectively account for the superior photocatalytic performance observed in the 10EuCN material.[58,59]

Fig. 9a and b illustrates the influence of different reactive species on the photocatalytic efficiency of EuCN, as investigated by employing specific scavengers. Both the degradation efficiency of methylene blue (Fig. 9a) and the H_2O_2 production rate (Fig. 9b) were significantly affected by the presence of selective scavengers, indicating the involvement of multiple reactive species in the photocatalytic process. In the MB degradation study (Fig. 9a), the removal efficiency under normal conditions (no scavenger) reached 93.91%. Upon the addition of BQ, the efficiency dropped to 63.31%, confirming that $^{\bullet}O_2^-$ plays a major role in MB degradation. A more pronounced suppression was observed with $AgNO_3$, an e^- scavenger, which reduced the degradation efficiency to 52.85%. This suggests that photogenerated electrons are critical for initiating the reduction pathways leading to the formation of reactive oxygen species. In contrast, the addition of EDTA had only a slight impact with a degradation efficiency of 90.97%, indicating that holes contribute marginally to this system. The mannitol scavenger also caused a moderate reduction in efficiency to 75.06%, implying a secondary role of $^{\bullet}OH$ in the degradation mechanism.

Fig. 9b further supports these findings by tracking H_2O_2 generation in the presence of different scavengers. The highest H_2O_2 concentration was observed with EDTA, suggesting that the scavenging of holes favors electron accumulation and promotes the two-electron reduction of O_2 to H_2O_2. In contrast, $AgNO_3$ significantly inhibited H_2O_2 formation, reaffirming the essential role of electrons in the reduction process. Remarkably, the presence of BQ almost completely suppressed H_2O_2 generation, underscoring the pivotal role of $^{\bullet}O_2^-$ as an intermediate in the H_2O_2 production pathway. The influence of mannitol was moderate, further confirming that $^{\bullet}OH$ radicals are not the dominant species in this system. Collectively, these results demonstrate that the photocatalytic mechanism of EuCN is primarily governed by $^{\bullet}O_2^-$ and electrons, with $^{\bullet}OH$ and h^+ playing secondary or minimal roles.

The band gap energy for each sample was determined using the Tauc plot formula, as illustrated in Fig. 9d. The calculation of the band gap energy was based on eqn (3).

$$\alpha h v = A\left(h v - E_g\right)^{\frac{n}{2}} \tag{3}$$

where α, h, v, A, E_g, and n are the absorption coefficient, Planck constant, light frequency, a constant, bandgap, and an

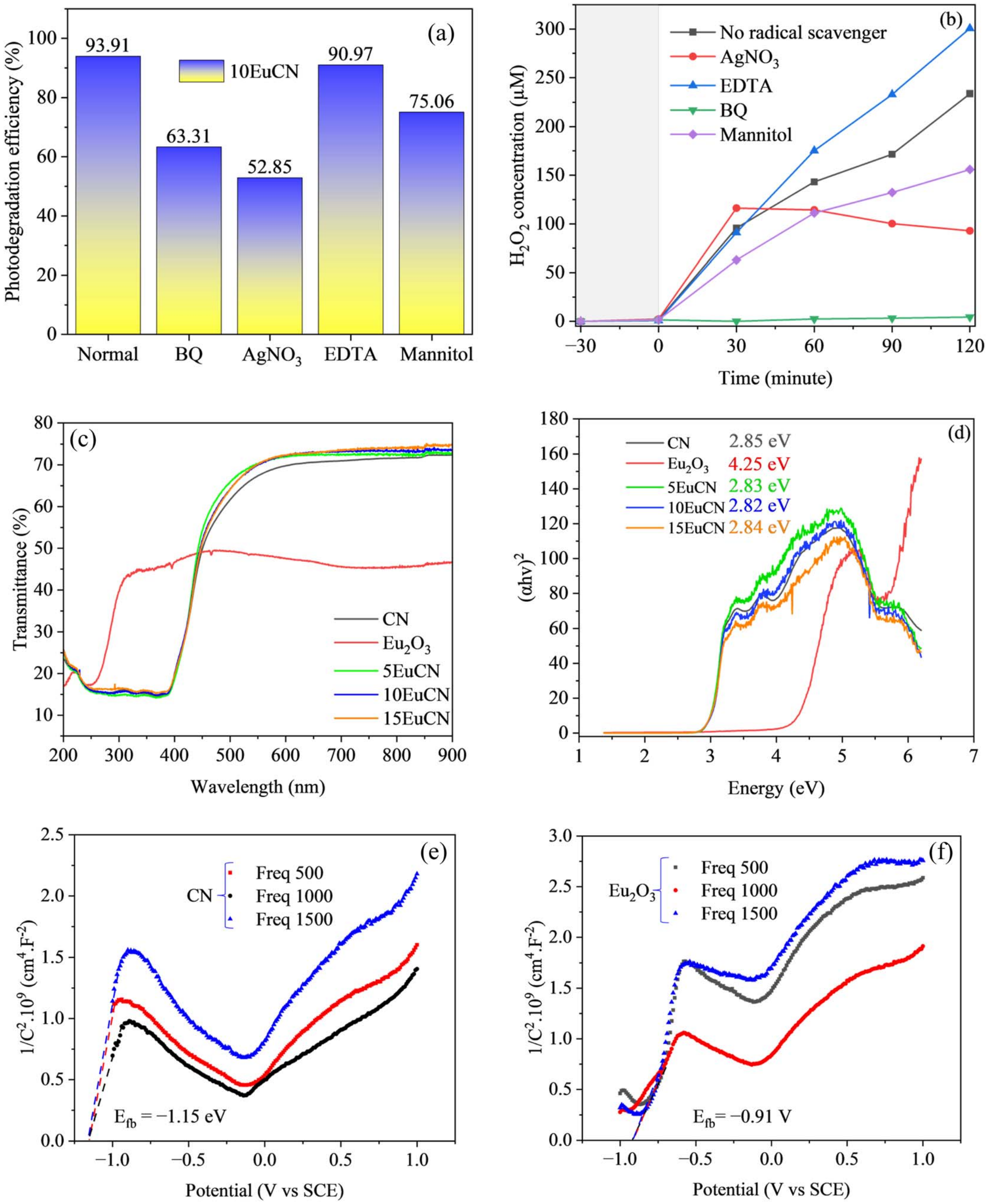

Fig. 9 Investigation of radical scavenging effects on (a) photodegradation of methylene blue and (b) photoproduction of hydrogen peroxide of the 10EuCN composite; (c) UV-DRS spectra, (d) bandgap values, and (c–f) Mott–Schottky curves of the materials.

exponent that depends on the nature of the electronic transition, respectively.

As illustrated in Fig. 9c and d, the optical band gap energies of CN, Eu_2O_3, and EuCN composites were estimated using Tauc plots. The band gap values of CN, Eu_2O_3, 5EuCN, 10EuCN, and 15EuCN were determined to be 2.85, 4.25, 2.83, 2.82, and 2.84 eV, respectively. Notably, the incorporation of Eu_2O_3 into the CN matrix led to a narrowing of the band gap, with 10EuCN exhibiting the lowest value (2.82 eV). This band gap reduction is attributed to the electronic interaction between Eu_2O_3 and CN, which introduces localized energy states and facilitates the formation of mid-gap levels. The resulting band structure modification enhances visible light absorption and promotes charge separation, both of which contribute to the improved photocatalytic performance of the EuCN composites. As shown in Fig. 9e and f, the Mott–Schottky curves of CN and Eu_2O_3 show that they are n-type semiconductors. Pristine CN exhibits $E_{fb} = -1.15$ V whereas Eu_2O_3 shows a less negative value at −0.91 V, indicating an upward shift in the conduction band edge upon the addition of Eu_2O_3. The EuCN composites display intermediate E_{fb} values that depend on the amount of Eu_2O_3 (Fig. S8a–c), with 10EuCN showing a well-matched band alignment

Table 4 Summary calculation of band gap energy, E_{VB}, and E_{CB} of Eu_2O_3 and CN

Materials	E_{CB} (eV)	E_{VB} (eV)	E_g (eV)
Eu_2O_3	−0.77	3.48	4.25
CN	−1.01	1.84	2.85

between CN and Eu_2O_3. This variation in flat band potential reflects changes in the surface electronic structure and the extent of band bending, which provides further support for the formation of a heterojunction at the interface between CN and Eu_2O_3. The resulting heterojunction favors directional charge separation and reduces the rate of charge carrier recombination. These consistent observations across the EuCN series confirm that Eu_2O_3 not only introduces new electronic states as evidenced by PL and EIS results but also influences the overall band structure of CN through interfacial electronic interaction. From the UV-DRS and Mott–Schottky results, the band positions of Eu_2O_3 and CN were calculated as shown in Table 4.

The interfacial electronic structure and orbital interaction of the materials calculated using DFT are presented in Fig. S9. The CN monolayer was modeled by cleaving a single layer from its bulk structure, adopting the tri-*s*-triazine topology as the most stable configuration among carbon nitride polymorphs. The optimized monolayer structure (Fig. S9a) consists of 14 atoms (6 C and 8 N), arranged periodically in the *x* and *y* directions, with a vacuum spacing of 30 Å along the *z*-axis to avoid artificial interlayer interactions. Upon full relaxation using a 30 × 30 × 30 Monkhorst–Pack *k*-point mesh and a mesh cutoff of 200 Ry, the lattice constants of CN were calculated to be $a = 7.117$ Å, $b = 7.042$ Å, $c = 6.040$ Å, with interaxial angles $\alpha = 90.0001°$, $\beta = 89.9981°$, and $\gamma = 120.8056°$. The C–N bond lengths range from 1.23 to 1.326 Å, consistent with sp^2-hybridized bonding in the conjugated framework. The Eu_2O_3 nanocluster was constructed by extracting two europium and three oxygen atoms from the cubic Eu_2O_3 bulk phase (materials project ID: mp-1182469), and positioned atop a (2 × 2) CN supercell with an interfacial distance of 4 Å. Structural optimization was carried out using a DZP basis set, a 3 × 3 × 1 *k*-point grid, and a mesh cutoff of 300 Ry. As shown in Fig. S9b and c, the resulting heterostructure exhibits localized structural distortion near the EuCN interface. In particular, the previously planar CN monolayer is visibly bent upward in the vicinity of the Eu and O atoms, indicating strong interfacial interaction. This distortion is consistent with the observed Eu–N and Eu–O bond lengths of 2.116–2.345 and 2.5 Å, respectively, and suggests that physical adsorption alone cannot account for the bonding, but rather partial orbital overlap and charge redistribution are responsible for the perturbation. Total DOS (density of states) analysis further reveals the electronic consequences of this structural coupling, as shown in Fig. S9d. Upon Eu_2O_3 loading, the band structure is notably modified, the bandgap becomes a pseudogap of 0.621 eV and Eu-derived 4f states dominate the region near the Fermi level. The distortion-induced orbital interaction likely contributes to the introduction of mid-gap states, effectively narrowing the bandgap and altering the carrier dynamics.

To examine the charge redistribution in the EuCN system, charge density difference calculations were carried out for two configurations: one with full relaxation of both CN (Fig. 10a) and one in which the CN layer was fixed while Eu_2O_3 was allowed to relax (Fig. 10b). In these maps, the yellow regions indicate where electrons accumulate, and the cyan regions show where electrons are depleted. In both cases, electrons are clearly transferred from Eu_2O_3 to CN. Electron depletion appears around Eu and O atoms, while electron accumulation is mostly seen near the C atoms in CN. The charge transfer tends to occur more strongly between the O atoms in Eu_2O_3 and the C atoms in CN rather than with N atoms. This suggests that the interaction at the interface is not purely physical but involves orbital overlap, especially between O 2p and C 2p orbitals. In the relaxed structure (Fig. 10a), the distortion at the interface further emphasizes this behavior. Although the fixed-CN structure (Fig. 10b) limits the degree of deformation, the same electron transfer trend is observed, which means that the direction of charge migration is not an artifact of geometry, but intrinsic to the system. Partial density of states (PDOS) shown in Fig. 10c supports this observation. The Fermi level is dominated by Eu 4f states, and these appear in the middle of the bandgap of CN. As a result, the bandgap becomes narrower and forms a pseudogap around 0.621 eV. The presence of mid-gap states related to Eu confirms that Eu not only perturbs the electronic structure of CN but also introduces localized levels that may act as temporary electron traps.

In addition, the work function analysis provides quantitative evidence for the intrinsic electronic interaction at the Eu_2O_3–CN interface. As shown in Fig. 10d, pristine CN exhibits a work function of 4.29 eV, whereas the EuCN composite displays a significantly reduced value of 2.60 eV (Fig. 10e). The marked decrease in work function after Eu_2O_3 decoration indicates spontaneous electron transfer from Eu_2O_3 to CN during interfacial contact, which is fully consistent with the charge density difference results (Fig. 10a and b). This electron redistribution leads to the formation of an interfacial dipole and modifies the electrostatic potential profile across the junction. The downward shift of the vacuum level in EuCN relative to pristine CN reflects a realignment of surface potential caused by charge accumulation on the CN side. Such a change confirms strong electronic coupling between the two components and suggests the establishment of a built-in internal electric field at the heterointerface. The significant work function reduction, therefore, not only demonstrates effective interfacial charge transfer but also provides solid theoretical support for the electronic structure reconstruction observed in the PDOS results, including the Fermi level shift and bandgap narrowing induced by Eu 4f states.

Based on the experimental results and analysis, the proposed photocatalytic mechanism for the EuCN composites is illustrated in Fig. 10f, which aligns with a S-scheme heterojunction configuration.[49,50] When Eu_2O_3 and CN are brought into contact, the difference in their work functions drives interfacial electron redistribution until the Fermi levels reach equilibrium. This charge migration induces band bending at the interface and establishes a built-in internal electric field

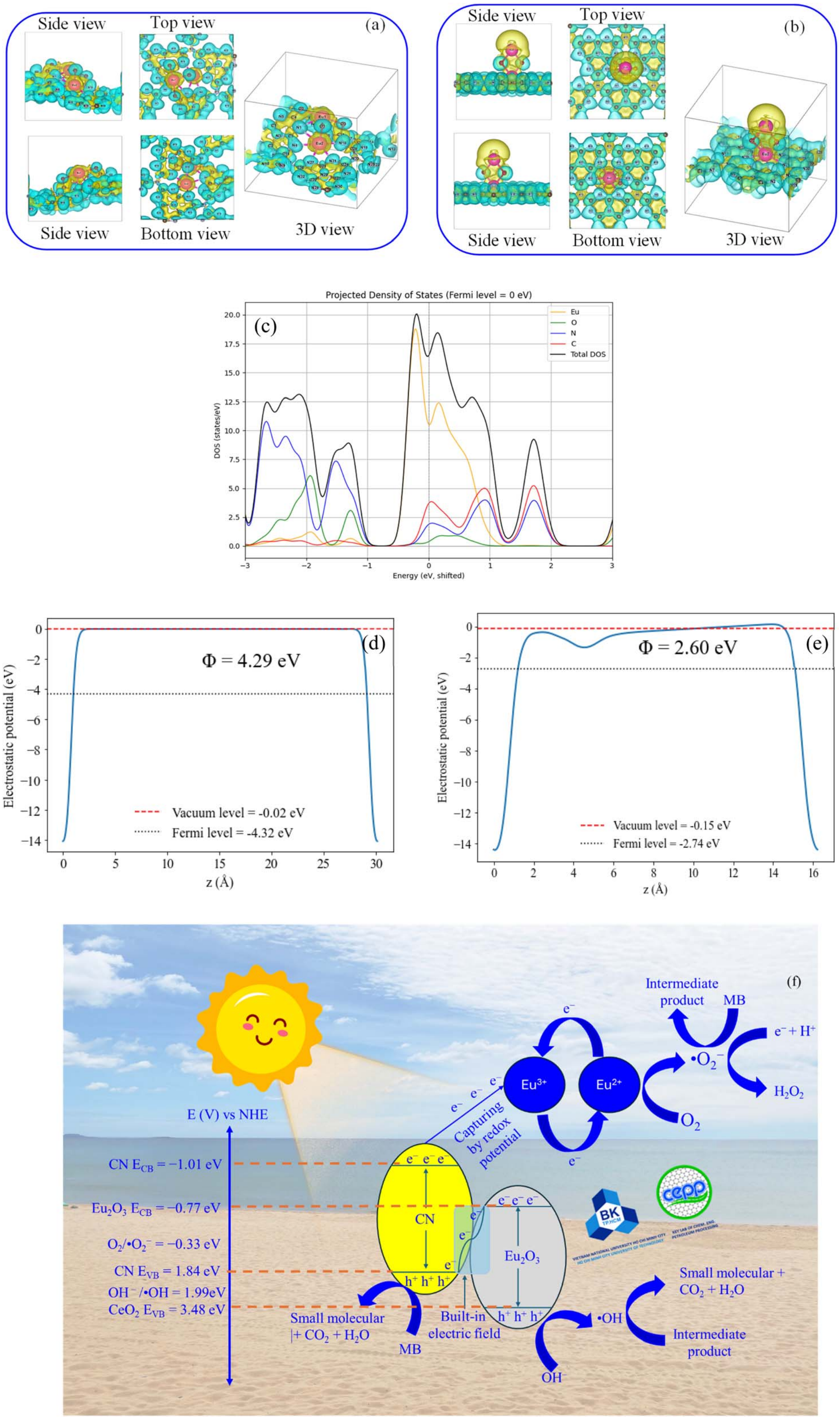

Fig. 10 Charge density maps of EuCN composites with (a) non-fixed and (b) fixed CN configuration; (c) PDOS for the constrained CN configuration in the EuCN composites; work function of (d) CN and (e) EuCN composite; and (f) possible photocatalytic mechanism of EuCN composites.

directed from the lower work function component to the higher work function component. The formation of this internal electric field is a key prerequisite for the S-scheme charge-transfer pathway. Under visible-light irradiation, both CN and Eu_2O_3 absorb photons, promoting the excitation of e^- from the valence band to the conduction band, thus generating e^-–h^+ pairs in both semiconductors. Driven by the band bending and internal electric field at the heterojunction interface, the photogenerated electrons in the conduction band of Eu_2O_3 preferentially recombine with the holes in the valence band of CN. This selective recombination pathway preserves the electrons in the conduction band of CN and the holes in the valence band of Eu_2O_3, both of which exhibit strong reduction and oxidation potentials, respectively. The electrons accumulated in the conduction band of CN possess sufficient reduction potential for O_2 activation, while the holes retained in the valence band of Eu_2O_3 exhibit strong oxidation capability toward organic pollutants. Moreover, the Eu^{3+}/Eu^{2+} redox couple further enhances charge separation and interfacial redox cycling. The 4f electronic configuration of europium provides localized energy states that function as transient electron traps. Electrons photogenerated in CN can be temporarily captured by Eu^{3+} and reduced to Eu^{2+}, followed by electron transfer to dissolved oxygen to generate $^{\bullet}O_2^-$ and create H_2O_2. Meanwhile, the holes in Eu_2O_3 oxidize surface hydroxyl groups or water molecules to produce $^{\bullet}OH$ radicals, contributing to the degradation of methylene blue into CO_2 and H_2O as well as sacrificial oxidation to provide more H^+ for H_2O_2 photoproduction.

4. Conclusions

In this work, the EuCN composite photocatalysts were successfully synthesized through a green and sustainable method, utilizing *Centella asiatica* leaf extract as a bio-reducing agent for the formation of europium oxide (Eu_2O_3), which was subsequently combined with graphitic carbon nitride (CN). The resulting composites exhibited remarkable photocatalytic performance, achieving 93.82% degradation of methylene blue under halogen lamp illumination and generating 233.73 μM of hydrogen peroxide under UV-LED irradiation. Detailed structural, morphological, and electronic characterization results confirmed the formation of a well-defined heterojunction between Eu_2O_3 and CN. Optical and photoelectrochemical characterization results, supported by radical-scavenging experiments as well as density functional theory calculations revealed that the enhanced photocatalytic performance arises from a S-scheme charge-transfer pathway that facilitates efficient charge separation while preserving robust redox potentials. Importantly, the EuCN composites demonstrated reliable performance over repeated cycles and strong operational durability. Coupled with a low-cost, environmentally friendly synthesis route and dual photocatalytic functions, these attributes underscore the material's practical applicability for real-world wastewater treatment and solar-driven oxidant generation. These findings highlight the novelty of this study in integrating green synthesis, structural engineering, and functional stability toward sustainable photocatalysis.

Conflicts of interest

The authors declare that they have no known competing financial interests or personal relationships that could have appeared to influence the work reported in this paper.

Data availability

All results generated or analysed during this study are fully presented in the manuscript.

Supplementary information (SI) is available. See DOI: https://doi.org/10.1039/d6su00035e.

Acknowledgements

This research was funded by Vietnam National University Ho Chi Minh City (VNU-HCM) under grant number NCM2025-20-01. We acknowledge Ho Chi Minh City University of Technology (HCMUT), VNU-HCM for supporting this study.

References

1 A. Raihan, The dynamic nexus between economic growth, renewable energy use, urbanization, industrialization, tourism, agricultural productivity, forest area, and carbon dioxide emissions in the Philippines, *Energy Nexus*, 2023, **9**, 100180, DOI: 10.1016/j.nexus.2023.100180.
2 P. O. Oladoye, T. O. Ajiboye, E. O. Omotola and O. J. Oyewola, Methylene blue dye: Toxicity and potential elimination technology from wastewater, *Results Eng.*, 2022, **16**, 100678, DOI: 10.1016/j.rineng.2022.100678.
3 U. Vishwa Priya, A. Saranya, T. S. N. Sankara Narayanan and K. Ravichandran, Photocatalytic removal of methylene blue *via* HAp/AGCN composites: Synergistic effects and mechanistic insights, *Environ. Res.*, 2025, **278**, 121582, DOI: 10.1016/j.envres.2025.121582.
4 R. Rashid, I. Shafiq, P. Akhter, M. J. Iqbal and M. Hussain, A state-of-the-art review on wastewater treatment techniques: the effectiveness of adsorption method, *Environ. Sci. Pollut. Res.*, 2021, **28**(8), 9050–9066, DOI: 10.1007/s11356-021-12395-x.
5 S. A. Aguilar-Maruri, R. Ocampo-Pérez, L. Ramos-Galicia, V. Collins-Martínez, G. Palestino and N. Sano, Photodegradation of methylene blue using carbonized bagasse doped with cerium oxide nanoparticles, *Environ. Res.*, 2025, **286**, 122977, DOI: 10.1016/j.envres.2025.122977.
6 A. Khan, H.-Y. Chen and C. Rusly, Visible-light-driven removal of mixed dye pollutants by a novel ZnO/CNT/GO ternary nanocomposite: Synergistic degradation of Congo red and methylene blue, *Environ. Res.*, 2025, **283**, 122156, DOI: 10.1016/j.envres.2025.122156.
7 S. R. Mishra, V. Gadore and M. Ahmaruzzaman, From light to chemicals: Breaking ground in photocatalytic H_2O_2 production for a sustainable future, *Mater. Today Sustain.*, 2024, **27**, 100819, DOI: 10.1016/j.mtsust.2024.100819.
8 P. Tordi, F. Ridi, P. Samorì and M. Bonini, Cation-Alginate Complexes and Their Hydrogels: A Powerful Toolkit for the

Development of Next-Generation Sustainable Functional Materials, *Adv. Funct. Mater.*, 2025, **35**(9), 2416390, DOI: 10.1002/adfm.202416390.

9 O. Iqbal, *et al.*, A review on the synthesis, properties, and characterizations of graphitic carbon nitride (g-C_3N_4) for energy conversion and storage applications, *Mater. Today Phys.*, 2023, **34**, 101080, DOI: 10.1016/j.mtphys.2023.101080.

10 M. Xu, J. Yang, C. Sun, L. Liu, Y. Cui and B. Liang, Performance enhancement strategies of bi-based photocatalysts: A review on recent progress, *Chem.–Eng. J.*, 2020, **389**, 124402, DOI: 10.1016/j.cej.2020.124402.

11 G. Z. S. Ling, S.-F. Ng and W.-J. Ong, Tailor-Engineered 2D Cocatalysts: Harnessing Electron–Hole Redox Center of 2D g-C3N4 Photocatalysts toward Solar-to-Chemical Conversion and Environmental Purification, *Adv. Funct. Mater.*, 2022, **32**(29), 2111875, DOI: 10.1002/adfm.202111875.

12 H. Li, Z. Guo, H. Azimi, M. Ebadi, A. Shirmardi and R. Yousefi, Rapid tetracycline degradation by S-scheme Se/g-C3N4 heterostructure, *J. Aust. Ceram. Soc.*, 2025, **61**(2), 569–580, DOI: 10.1007/s41779-024-01088-6.

13 F. Xie, *et al.*, Synergistic effect of cobalt-induced phase transition and S-scheme heterojunction engineering for photothermal-enhanced photocatalytic hydrogen production over ZnIn2S4/Co0.15Fe0.85S2, *Chem. Eng. J.*, 2026, **529**, 172997, DOI: 10.1016/j.cej.2026.172997.

14 R. Zhang, *et al.*, Interfacial CoS bond-enhanced Mn0.3Cd0.7S/CoPB Schottky junction for photothermal-assisted photocatalytic hydrogen evolution, *J. Colloid Interface Sci.*, 2026, **703**, 139176, DOI: 10.1016/j.jcis.2025.139176.

15 S. Li, *et al.*, Self-floating Bi4O5Br2/P-doped C3N4/carbon fiber cloth with S-scheme heterostructure for boosted photocatalytic removal of emerging organic contaminants, *Chinese J. Catal.*, 2025, **76**, 37–49, DOI: 10.1016/S1872-2067(25)64780-2.

16 C. You, *et al.*, Plasmonic effect augmented S-scheme mechanism in Ag/Ag2O/C3N5 photocatalyst enables efficient photocatalytic degradation of antibiotics, *J. Mater. Sci. Technol.*, 2026, **242**, 64–74, DOI: 10.1016/j.jmst.2025.05.002.

17 H. Qian, *et al.*, Flexible Room-Temperature Ammonia Sensor Using Multi-Heterojunction MoO3/CuO/Cu2O Nanoclusters for Noninvasive Kidney Disease Diagnosis, *Small Struct.*, 2025, 2400549, DOI: 10.1002/sstr.202400549.

18 Q. D. Ho, V. D. Lai, Q. A. Nguyen, D. N. Vu, T. K. L. Dang and D. D. La, Green synthesis of g-C3N4/CeO2 nanocomposites for enhanced photocatalytic degradation of organic dye under simulated sunlight, *Diam. Relat. Mater.*, 2025, **157**, 112484, DOI: 10.1016/j.diamond.2025.112484.

19 Y. Chen, D. Ren, C. Deng, J. Zhong, L. Dou and S. Huang, Rationally construction of Dy2O3/g-C3N4 heterojunctions with largely enhanced photocatalytic hydrogen evolution activity, *Mater. Res. Bull.*, 2024, **179**, 112971, DOI: 10.1016/j.materresbull.2024.112971.

20 X. Jing, *et al.*, Enhancing Dy2O3/g-C3N4 visible photocatalytic hydrogen production performance by loading graphene-like carbon from Enteromorpha prolifera (EP-GL), *J. Alloys Compd.*, 2024, **984**, 173964, DOI: 10.1016/j.jallcom.2024.173964.

21 Z. Li, *et al.*, Electrically induced quenching effect in photoluminescence devices composed of Eu3+-complex-doped polyethylene oxide, *J. Alloys Compd.*, 2025, **1014**, 178492, DOI: 10.1016/j.jallcom.2025.178492.

22 Z. Ullah, *et al.*, Unveiling Biodiesel Production: Exploring Reaction Protocols, Catalysts, and Influential Factors, *ChemBioEng Rev.*, 2024, **11**(6), e202400028, DOI: 10.1002/cben.202400028.

23 M. A. Dheyab, *et al.*, Recent advances of plant-mediated metal nanoparticles: Synthesis, properties, and emerging applications for wastewater treatment, *J. Environ. Chem. Eng.*, 2024, **12**(2), 112345, DOI: 10.1016/j.jece.2024.112345.

24 T. K. N. Tran, H. T. V. Nguyen, T. T. H. Nguyen and T. C. Thai, Phytochemical screening and biological activity of *Centella asiatica* (L.) Urban extracts by different methods, *J. Hortic. Postharvest Res.*, 2025, 351–364.

25 S. Tripathy and P. P. Srivastav, Maize starch and β-cyclodextrin nanocarriers for encapsulation of Centella asiatica polyphenols: synthesis, physicochemical properties, and pH-responsive delivery, *Food Chem.*, 2026, **507**, 148202, DOI: 10.1016/j.foodchem.2026.148202.

26 M. H.-O. Rashid, *et al.*, Antioxidant, cytotoxic, antibacterial and thrombolytic activities of *Centella asiatica* L.: possible role of phenolics and flavonoids, *Clin. Phytosci.*, 2023, **9**(1), 1, DOI: 10.1186/s40816-023-00353-8.

27 T. Dang Khoa, *et al.*, Synthesis of tin selenide nanoparticles using Polygonum avicular extract decorated on graphitic carbon nitride for enhancing photodegradation of amoxicillin trihydrate and photoproduction of hydrogen peroxide, *Mater. Chem. Phys.*, 2025, **329**, 130032, DOI: 10.1016/j.matchemphys.2024.130032.

28 M. raj S. Nivetha, *et al.*, Construction of SnO2/g-C3N4 an effective nanocomposite for photocatalytic degradation of amoxicillin and pharmaceutical effluent, *Environ. Res.*, 2022, **209**, 112809, DOI: 10.1016/j.envres.2022.112809.

29 J.-G. Kang, Y. Jung, B.-K. Min and Y. Sohn, Full characterization of Eu(OH)3 and Eu2O3 nanorods, *Appl. Surf. Sci.*, 2014, **314**, 158–165, DOI: 10.1016/j.apsusc.2014.06.165.

30 S. M. Abdel Moneim, T. A. Gad-Allah, M. F. El-Shahat, A. M. Ashmawy and H. S. Ibrahim, Novel application of metal-free graphitic carbon nitride (g-C3N4) in photocatalytic reduction—Recovery of silver ions, *J. Environ. Chem. Eng.*, 2016, **4**(4), 4165–4172, DOI: 10.1016/j.jece.2016.08.034.

31 Z. Zhang, K. Liu, Z. Feng, Y. Bao and B. Dong, Hierarchical Sheet-on-Sheet ZnIn2S4/g-C3N4 Heterostructure with Highly Efficient Photocatalytic H2 production Based on Photoinduced Interfacial Charge Transfer, *Sci. Rep.*, 2016, **6**(1), 19221, DOI: 10.1038/srep19221.

32 S. Li, X. Li, Y. Liu, P. Zhang, J. Zhang and B. Zhang, Interfacial engineering of a plasmonic Ag/Ag2CO3/C3N5 S-scheme heterojunction for high-performance

photocatalytic degradation of antibiotics, *Chinese J. Catal.*, 2025, **72**, 130–142, DOI: 10.1016/S1872-2067(25)64652-3.

33 C.-H. Zeng, *et al.*, Synthesis of Porous Europium Oxide Particles for Photoelectrochemical Water Splitting, *Electrochim. Acta*, 2015, **165**, 396–401, DOI: 10.1016/j.electacta.2015.03.046.

34 S. Kumar, R. Prakash, R. J. Choudhary and D. M. Phase, Structural, XPS and magnetic studies of pulsed laser deposited Fe doped Eu2O3 thin film, *Mater. Res. Bull.*, 2015, **70**, 392–396, DOI: 10.1016/j.materresbull.2015.05.007.

35 S. Nayak, L. Mohapatra and K. Parida, Visible light-driven novel g-C3N4/NiFe-LDH composite photocatalyst with enhanced photocatalytic activity towards water oxidation and reduction reaction, *J. Mater. Chem. A*, 2015, **3**(36), 18622–18635, DOI: 10.1039/C5TA05002B.

36 E. Parvizi, *et al.*, Photocatalytic efficacy of supported tetrazine on MgZnO nanoparticles for the heterogeneous photodegradation of methylene blue and ciprofloxacin, *RSC Adv.*, 2019, **9**(41), 23818–23831, DOI: 10.1039/C9RA04702F.

37 F. Chen, Z. Liu, Y. Liu, P. Fang and Y. Dai, Enhanced adsorption and photocatalytic degradation of high-concentration methylene blue on Ag2O-modified TiO2-based nanosheet, *Chem.–Eng. J.*, 2013, **221**, 283–291, DOI: 10.1016/j.cej.2013.02.019.

38 A. K. Subramani, K. Byrappa, S. Ananda, K. M. Lokanatha Rai, C. Ranganathaiah and M. Yoshimura, Photocatalytic degradation of indigo carmine dye using TiO2 impregnated activated carbon, *Bull. Mater. Sci.*, 2007, **30**(1), 37–41, DOI: 10.1007/s12034-007-0007-8.

39 M. Cheng, *et al.*, Catalytic activity of iron species in layered clays for photodegradation of organic dyes under visible irradiation, *Appl. Catal., B*, 2008, **77**(3), 355–363, DOI: 10.1016/j.apcatb.2007.08.006.

40 Q. Zhang, T. Wang, Y. He, S. Zuo, Z. Zhao and L. Zhang, Large-scale preparation of N-doped microporous-dominated carbon-based adsorbents for efficient removal of Chromium(VI): The synergistic effect of different nitrogen configurations, *Clean. Water*, 2024, **1**, 100013, DOI: 10.1016/j.clwat.2024.100013.

41 L. Chen, *et al.*, A incorporation of metal into worm-like mesoporous silica materials for selective adsorption of MB in dyestuff, *J. Mol. Liq.*, 2024, **400**, 124585, DOI: 10.1016/j.molliq.2024.124585.

42 Z. Sun, H. Chen, L. Zhang, D. Lu and P. Du, Enhanced photocatalytic H2 production on cadmium sulfide photocatalysts using nickel nitride as a novel cocatalyst, *J. Mater. Chem. A*, 2016, **4**(34), 13289–13295, DOI: 10.1039/C6TA04696G.

43 M. Gu, Y. Yang, L. Zhang, B. Zhu, G. Liang and J. Yu, Efficient sacrificial-agent-free solar H2O2 production over all-inorganic S-scheme composites, *Appl. Catal., B*, 2023, **324**, 122227, DOI: 10.1016/j.apcatb.2022.122227.

44 A. A. Isari, F. Hayati, B. Kakavandi, M. Rostami, M. Motevassel and E. Dehghanifard, N, Cu co-doped TiO2@functionalized SWCNT photocatalyst coupled with ultrasound and visible-light: An effective sono-photocatalysis process for pharmaceutical wastewaters treatment, *Chem. Eng. J.*, 2020, **392**, 123685, DOI: 10.1016/j.cej.2019.123685.

45 W. Han, *et al.*, Enhanced photocatalytic activities of three-dimensional graphene-based aerogel embedding TiO2 nanoparticles and loading MoS2 nanosheets as Co-catalyst, *Int. J. Hydrogen Energy*, 2014, **39**(34), 19502–19512, DOI: 10.1016/j.ijhydene.2014.09.043.

46 J. Lin, *et al.*, Functional Carbon Nitride Materials in Photo-Fenton-Like Catalysis for Environmental Remediation, *Adv. Funct. Mater.*, 2022, **32**(24), 2201743, DOI: 10.1002/adfm.202201743.

47 R.-K. Ye, *et al.*, Surface engineering of hematite nanorods by 2D Ti3C2-MXene: Suppressing the electron-hole recombination for enhanced photoelectrochemical performance, *Appl. Catal., B*, 2021, **291**, 120107, DOI: 10.1016/j.apcatb.2021.120107.

48 R. Du, *et al.*, Controlled oxygen doping in highly dispersed Ni-loaded g-C3N4 nanotubes for efficient photocatalytic H2O2 production, *Chem.–Eng. J.*, 2022, **441**, 135999, DOI: 10.1016/j.cej.2022.135999.

49 Y. Yang, *et al.*, Ti3C2 Mxene/porous g-C3N4 interfacial Schottky junction for boosting spatial charge separation in photocatalytic H2O2 production, *Appl. Catal., B*, 2019, **258**, 117956, DOI: 10.1016/j.apcatb.2019.117956.

50 Y. Shiraishi, *et al.*, Sunlight-Driven Hydrogen Peroxide Production from Water and Molecular Oxygen by Metal-Free Photocatalysts, *Angew. Chem., Int. Ed.*, 2014, **53**(49), 13454–13459, DOI: 10.1002/anie.201407938.

51 S. Iqbal, *et al.*, Z-scheme design of hydrothermally synthesized Sm-Fe-doped LaNiO3/g-C3N4 heterostructure photo-catalyst for the efficient elimination of methylene blue & moxifloxacin pollutants, *Polyhedron*, 2025, **270**, 117446, DOI: 10.1016/j.poly.2025.117446.

52 Z. Chu, *et al.*, CeO2-g-C3N4 S-scheme heterojunctions for enhanced photocatalytic performance: Effects of surface C/N ratio on photocatalytic and adsorption properties, *Composites, Part B*, 2023, **257**, 110689, DOI: 10.1016/j.compositesb.2023.110689.

53 S. Li, *et al.*, Floatable S-scheme Bi4O5Br2/C3N4/Carbon Fiber Cloth with Robust Internal Electric Field for Efficient Photocatalytic Antibiotic Decontamination, *Adv. Fiber Mater.*, 2025, **7**(6), 2032–2047, DOI: 10.1007/s42765-025-00601-1.

54 S. Khan, H.-W. Zheng, H. Jiao, S. Saleem, Z. Gul, J. Y. Al-Humaidi, A. Al Bahir, R. H. Althomali, A. Ali and M. M. Rahman, Reduction mechanism and energy transfer between Eu^{3+} and Eu^{2+} in Eu-doped materials synthesized in air atmosphere, *Rev. Inorg. Chem.*, 2024, **44**(4), 547–567, DOI: 10.1515/revic-2024-0011.

55 M. I. Ustinova, *et al.*, A europium shuttle for launching perovskites to space: using Eu2+/Eu3+ redox chemistry to boost photostability and radiation hardness of complex lead halides, *J. Mater. Chem. A*, 2024, **12**(22), 13219–13230, DOI: 10.1039/D3TA07598B.

56 J. J. Joos, P. F. Smet, L. Seijo and Z. Barandiarán, Insights into the complexity of the excited states of Eu-doped

luminescent materials, *Inorg. Chem. Front.*, 2020, **7**(4), 871–888, DOI: 10.1039/C9QI01455A.

57 D. Janardhana, S. N. Jayaramu, E. Coetsee, D. E. Motaung and H. C. Swart, Nanosheet g-C3N4 decorated α-Bi2O3:Eu3+ needles for efficient photocatalytic degradation of rhodamine B dye, *Mater. Sci. Semicond. Process.*, 2024, **184**, 108789, DOI: 10.1016/j.mssp.2024.108789.

58 T. Oshima, *et al.*, Two-Dimensional Perovskite Oxynitride K2LaTa2O6N with an H+/K+ Exchangeability in Aqueous Solution Forming a Stable Photocatalyst for Visible-Light H2 Evolution, *Angew. Chem., Int. Ed.*, 2020, **59**(24), 9736–9743, DOI: 10.1002/anie.202002534.

59 P. Mohan, *et al.*, BiVO4/SnS2 S-scheme heterojunction for improved photocatalytic performance under visible light: charge carrier mechanism validation by DFT and electrochemical studies, *Appl. Phys. A*, 2025, **131**(12), 967, DOI: 10.1007/s00339-025-09039-z.